Schuessler, J.A.; von Blanckenburg, F. (2014) Testing the limits of micro-scale analyses of Si stable isotopes by femtosecond laser ablation multicollector inductively coupled plasma mass spectrometry with application to rock weathering *Spectrochimica Acta Part B: Atomic Spectroscopy*, 98, 1-18

DOI: 10.1016/j.sab.2014.05.002

# Testing the limits of micro-scale analyses of Si stable isotopes by femtosecond laser ablation multicollector inductively coupled plasma mass spectrometry with application to rock weathering

Jan A. Schuessler*, Friedhelm von Blanckenburg

*GFZ German Research Centre for Geosciences, Section 3.4 Earth Surface Geochemistry, Telegrafenberg, D-14473 Potsdam, Germany*
**corresponding author (jan.schuessler@gfz-potsdam.de)*

**Please cite this article as:**

Jan A. Schuessler, Friedhelm von Blanckenburg.

Testing the limits of micro-scale analyses of Si stable isotopes by femtosecond laser ablation multicollector inductively coupled plasma mass spectrometry with application to rock weathering,

**Spectrochimica Acta Part B: Atomic Spectroscopy** (2014), 98, 1-18

**doi: 10.1016/j.sab.2014.05.002**

Keywords: Femtosecond laser ablation, MC-ICP-MS, stable isotopes, Si isotopes, weathering

**Abstract.** An analytical protocol for accurate in-situ Si stable isotope analysis has been established on a new second-generation custom-built femtosecond laser ablation system. The laser was coupled to a multicollector inductively coupled plasma mass spectrometer (fsLA-MC-ICP-MS). We investigated the influence of laser parameters such as spot size, laser focussing, energy density and repetition rate, and ICP-MS operating conditions such as ICP mass load, spectral and non-spectral matrix effects, signal intensities, and data processing on precision and accuracy of Si isotope ratios. We found that stable and reproducible ICP conditions were obtained by using He as aerosol carrier gas mixed with $Ar/H_2O$ before entering the plasma. Precise $\delta^{29}Si$ and $\delta^{30}Si$ values (better than ±0.23‰, 2SD) can be obtained if the area ablated is at least 50 x 50 µm; or, alternatively, for the analysis of geometric features down to the width of the laser spot (about 20 µm) if an equivalent area is covered. Larger areas can be analysed by rastering the laser beam, whereas small single spot analyses reduce the attainable precision of $\delta^{30}Si$ to ca. ±0.6 ‰, 2SD, for <30 µm diameter spots. It was found that focussing the laser beam beneath the sample surface with energy densities between 1 and 3.8 J/cm² yields optimal analytical conditions for all materials investigated here. Using pure quartz (NIST 8546 aka. NBS-28) as measurement standard for calibration (standard-sample-bracketing) did result in accurate and precise data of international reference materials and samples covering a wide range in chemical compositions (Si single crystal IRMM-017, basaltic glasses KL2-G, BHVO-2G and BHVO-2, andesitic glass ML3B-G, rhyolitic glass ATHO-G, diopside glass JER, soda-lime glasses NIST SRM 612 and 610, San Carlos olivine). No composition-dependent matrix effect was discernible within uncertainties of the method. The method was applied to investigate the Si isotope signature of rock weathering at the micro-scale in a corestone sampled from a highly weathered roadcut profile in the tropical Highlands of Sri Lanka. The results show that secondary weathering products accumulated in cracks and grain boundaries are isotopically lighter than their unweathered plagioclase host, consistent with isotopically heavy dissolved Si found in rivers.

## 1. Introduction

Laser ablation inductively coupled plasma mass spectrometry (LA-ICP-MS) is a powerful technique used to determine element concentrations and isotopic ratios in solid samples at a resolution of micrometres. The technique is now routinely applied in geological, archaeological, environmental, and biological studies. A prerequisite for the determination of both concentrations and isotope ratios is the need for accurate calibration. This prerequisite poses a formidable challenge because fractionation of both element and isotope ratios occurs during analysis. To determine optimised conditions, the influence of operating conditions of the laser and the ICP-MS on elemental and isotopic fractionation during LA-ICP-MS has been extensively studied in the past, in particular for trace element concentration or radiogenic isotope ratio measurements. Despite these efforts that were made during the past decades (e.g., see reviews by [1-7]), the fundamental causes for these fractionation effects are still not well understood. Hence, no unifying theory enabling quantitative prediction of routine analytical conditions is available to analysts who rely on empirically mapping-out reproducible operating conditions instead.

At the same time, new applications for LA-ICP-MS have arisen in the form of metal and metalloid stable isotope ratios in oceanography [8], environmental sciences [9], plant physiology [10], igneous petrology [11], and cosmochemistry [12], for example. These elements are subject to minor shifts in their relative isotope ratios that mostly amount to only a few permil (‰) or less per mass unit. To resolve these minor shifts, the analysis of these isotope ratios requires extremely high accuracy and precision. Whilst the measurements of these elements by "conventional" solution nebulisation MC-ICP-MS after chemical separation of the element of interest from their matrix is now close to routine for a range of elements, their analysis by laser ablation is still in its infancy.

The challenge that arises in the analysis of these isotope ratio measurements is that the limit to their accuracy is caused by bias at different stages of the analysis: from laser ablation, over particle formation and transport, atomisation/ionisation of particles, extraction of ions through the ICP-interface into the vacuum of the mass spectrometer, and ion detection. Hence, in order to obtain accurate and precise isotope ratios by LA-ICP-MS, a correction of these mass discrimination effects is necessary. Many of these issues have been resolved for the measurements of radiogenic isotope ratios, where a reference isotope ratio of the same element is available for internal correction. Such correction is not possible when stable isotope ratios shall be determined, where measurements in the shifts in abundance of all isotopes of a given elements relative to each other is the aim. Such stable isotope ratio measurements commonly rely on external mass bias correction by means of a standard-sample-bracketing approach [13, 14], where a reference material (typically an international measurement standard defined as δ-zero material by international agreement) is analysed before and after each unknown sample for time-interpolated mass bias correction. The fundamental prerequisite for this technique is that unknown samples are subject to an identical systematic bias during analyses as that affecting the reference material used for calibration (e.g., see [15] for an illustration of the concept). In solution ICP-MS this aim is achieved by chemical pre-concentration and introduction of the dissolved analyte into the ICP source at high purity.

In LA-ICP-MS analysis, this approach is not possible, and differences in chemical or physical properties between samples and reference material used for calibration were found to induce systematic errors (e.g., review by [7]). Such so-called matrix effects do affect the accuracy and precision of measured isotope ratios. Some elements have shown to be more prone to be affected than others. One established strategy is the use of matrix-matched reference materials of close resemblance to the samples in their physical and chemical properties for calibration, the analysis of which is subject to an identical systematic bias. However, appropriate reference materials covering the entire compositional range of geological or environmental samples are not always readily available. Hence, the ability to perform accurate measurement results without the need to employ matrix-matched reference material for calibration is highly desirable. Secondary ion mass spectrometry (SIMS) has emerged in the past years as another powerful technique for in-situ micro analysis of metal and metalloid stable isotopes. Similar to LA-ICP-MS, SIMS requires an equally careful correction of composition-dependent matrix effects, e.g., [16, 17].

In this regard the use of femtosecond (fs) lasers has been shown to be advantageous over nanosecond (ns) lasers due to minimised thermal ablation effects, leading to reduced laser-induced matrix effects [15, 19-23]. However, even if the laser-induced aerosol generation entails a strongly reduced bias, fs-LA analyses are still subject to mass bias generated when the aerosol enters the ICP interface (see above). Hence, the development of robust and widely available fs-LA-MC-ICP-MS procedures, together with a better understanding of the fundamental processes involved, and the characterisation of samples suitable for inter-laboratory comparison is a requirement for advancing the field of in-situ metal and metalloid stable isotope analyses.

We present here advances in micro-scale analyses of metal and metalloid stable isotopes using a second generation custom-built femtosecond laser ablation system coupled to a multicollector ICP mass spectrometer. The aim of this contribution is to map out optimum analytical conditions for fsLA-MC-ICP-MS measurements of stable Si isotope ratios covering a wide range of geological materials. Based on these findings an analytical protocol for accurate stable Si isotope analysis is established and quality control parameters as well as data acceptance/rejection criteria are defined. We present data on widely available and well-characterised reference materials suitable for inter-laboratory comparison. Because Si is a major element that is cycled in large amounts through the Earth's surface, we then present an application of the method to the study of the alteration of rocks and its minerals by weathering.

## 2. Materials and methods

### 2.1 Samples and sample preparation

To investigate the capabilities of laser ablation Si isotope analyses we used a range of different reference materials (glasses or mineral fragments). These are well-characterised in terms of their chemical composition and their Si isotope ratios. Reference values were used as reported in previous publications [12, 24-39]. Where such reports were lacking, reference Si isotope ratios were determined for this study by conventional solution MC-ICP-ICP analyses. For laser ablation samples were presented either in the form of petrographic thin sections or polished epoxy mounts. The reference material NIST8546 (hereafter referred to as NBS-28) is the international 'δ-zero' isotope measurement standard for Si isotopes. Grain mounts of NBS-28 quartz crystals were used directly as measurement standard for bracketing in most of the Si isotope analyses by laser ablation, unless stated otherwise. The MPI-DING glasses KL2-G, ML3B, ATHO-G are of basaltic, andesitic and rhyolitic composition, respectively [24]. NIST SRM 612 and 610 glasses are commonly used as a reference material for calibration in concentration measurements by laser ablation ICP-MS [40]. JER is a synthetic diopside glass ($CaMgSi_2O_6$) [25, 41]. BHVO-2G and BHVO-2 are basaltic reference materials used widely by geochemical laboratories. Both are therefore to date the most frequently analysed reference materials for Si isotopes. Whereas BHVO-2G is already supplied in the form of a glass by USGS, BHVO-2 is a basaltic rock powder. From this powder glass beads were prepared for laser ablation analysis using an Ir strip heater at MPI Mainz, Germany [42]. IRMM-017 is a single crystal made of pure Si and has been included in the sample selection as it features physical properties that are distinct from translucent silicate glasses and minerals. Fragments of olivine crystals ($Fo_{90}$, analysis from [43]) were taken from a xenolith from the San Carlos (SC) volcanic field in the south-western United States. These olivine crystals differ from the silicate glasses by their contrasting structural and chemical properties.

In an innovative application, we investigated the Si isotope signature of rock weathering at the micro-scale. A corestone sampled from a saprolite roadcut profile in the Highlands of Sri Lanka [44] was selected, from which petrographic thin sections (48 x 55 mm) were prepared with a sample thickness of 30 µm. To test for appropriate thin section preparation techniques, two thin sections were prepared from the same corestone sample. One thin section was prepared using a wet grinding/polishing technique (HakCore5), and the other using dry preparation (HakCore5b).

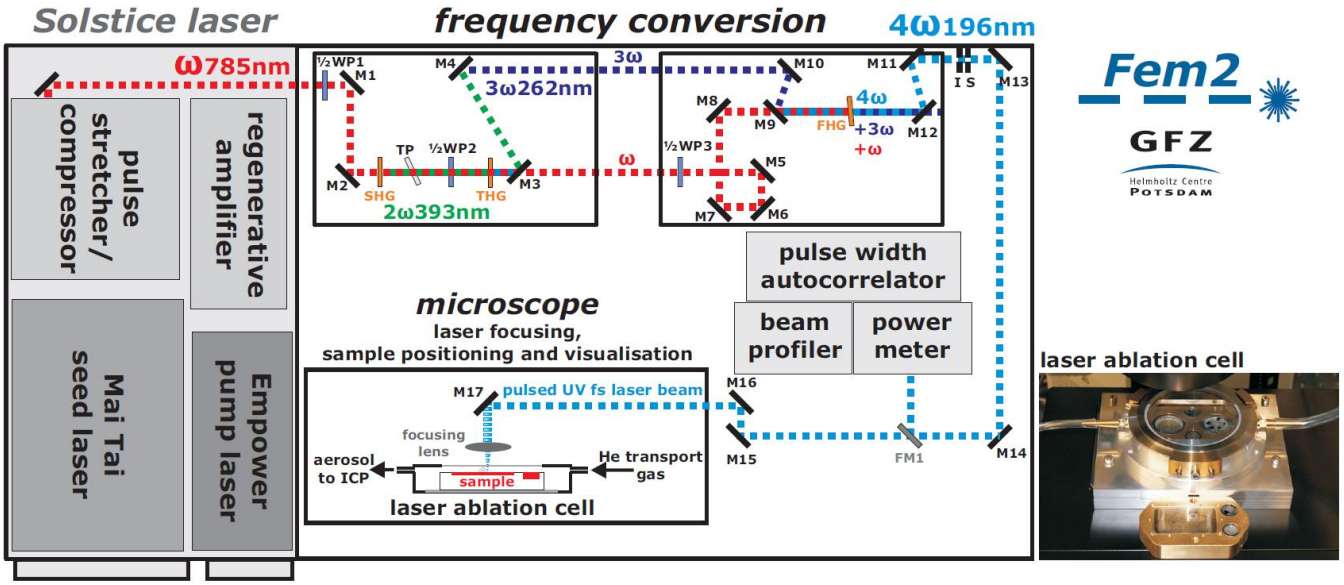


Figure 1. Schematic representation of the custom-built laser ablation system (Fem2) at GFZ Potsdam. The beam path (stippled lines) is shown from the infrared output (ω = 785 nm) port of the Solstice regenerative amplifier through subsequent frequency conversion to UV wavelength via barium betaborate crystals (SHG, THG, FHG). After passing an adjustable iris aperture (I) and computer-controlled shutter (S), the UV beam (4ω = 196 nm) is steered into a modified microscope (Olympus BX-61) by five UV-mirrors (M13 to M17) and focused through a lens-triplet into the ablation cell. A flip-mirror (FM1) can be placed in the UV-beam path to steer the laser beam to different beam diagnostic instruments (beam profiler, autocorrelator, power meter). The beam diagnostics instruments can also be placed at any position along the beam path by movable mirrors (not shown). The photograph shows the laser ablation cell. The cell can accommodate samples of various shape and size into different sample holders, whilst maintaining a constant geometry and free volume inside the chamber. The photograph shows 1 inch and ½ inch round samples mounted inside the cell and the exchangeable sample holder inset for a rectangular thin section and two ½ inch round samples in front of the cell.

2.2 Laser ablation system

We utilised an in-house built ultraviolet (UV) laser ablation (LA) system, incorporating the latest generation femtosecond (fs) Ti:sapphire regenerative amplifier system *Spectra Physics Solstice* as a laser source. The system provides full control over laser parameters, such as spot size, energy density, pulse width, repetition rate (from 1 to 1000 Hz), and beam shape. The spot size can be varied from 10 to 80 µm in diameter with resulting energy densities on the sample between 0.1 and 50 J/cm². A custom-designed software provides integrated control of laser parameters, sample positioning and observation, as well as fully automated analyses of up to several hundred analyses through a synchronised operation with the mass spectrometer.

The design of the system is comparable to UV fsLA systems established in other laboratories, which are based on a Ti:sapphire amplifier with subsequent wavelength conversion to UV [15, 18, 20, 45-47]. The specifics of the laser ablation system are described in the following. To produce ultrashort pulses with an energy of several millijoules the system combines a low-energy Ti:saphire femtosecond seed laser (< 100 fs, *Spectra Physics MaiTai*) and a high energy Nd:YLF pump laser (1 kHz, *Spectra Physics Empower-30*) in a regenerative amplifier. The amplification of short low-energy laser pulses with intensities of millijoule levels is achieved in the *Spectra Physics Solstice* regenerative amplifier by Chirped Pulse Amplification in a Ti:sapphire crystal, which produces infrared (IR) laser pulses with up to 3.5 mJ/pulse. The pulse width of the IR wavelength was measured by autocorrelation (*Spectra Physics PulseScout LR*) and was found to be 98 fs. Non-linear optics are used to convert the fundamental IR wavelength into the UV with a wavelength of 196 nm. This conversion is achieved by frequency doubling of the fundamental wavelength (ω = 785 nm) in a BBO (Barium Beta Borate) crystal to attain 2ω = 393 nm (Second Harmonic Generation, <0.8 mJ/pulse). The Third Harmonic Generation (THG), uses the SHG wavelength (2ω = 393 nm) in a second BBO crystal to produce 3ω = 262 nm (<0.7 mJ/pulse). Finally, the deep ultraviolet wavelength of 196 nm (<0.08 mJ/pulse), which is used for laser ablation, is obtained by sum-frequency generation, i.e. nonlinear combination of 262 nm with the fundamental wavelength 785 nm in a third BBO crystal.

The beam delivery of the UV laser beam onto the sample surface is custom-built on a vibration-damped optical breadboard table. After the Fourth Harmonic Generation, the laser beam is passed through an adjustable iris aperture (1 to 8 mm diameter) and then steered into a fully automated and computer controlled microscope (Olympus BX-61) by four 45° dielectric mirrors with a UV high reflection coating (>97%). The laser beam is then focused by an achromatic lens-triplet (fused silica-calcium fluoride, UV anti-reflection coating) into the sample contained in a He-flushed sample cell, which is mounted on a computer-controlled x, y, z stage. The compound lens has a focal length of 22.7 mm (N.A. 0.13) at 196 nm. The lens was developed (*Befort Optical Design*, Wetzlar, Germany) for our laser ablation system to minimise energy loss and pulse broadening during transmission and focussing of the UV laser beam. In its design, special emphasis was given to high-quality optical imaging of the sample, whilst maintaining an optimum laser beam quality.

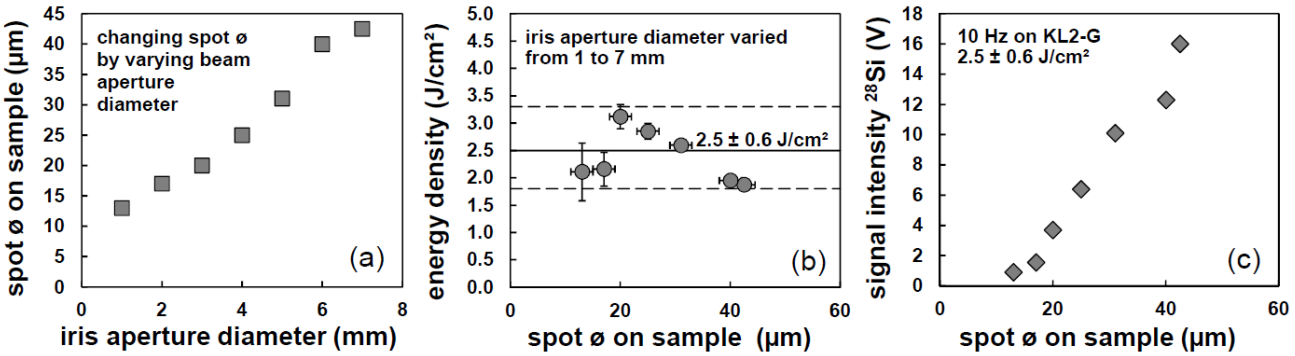


Figure 2. (a) The laser spot diameter on the sample surface can be varied by a variable iris aperture. (b) Due to the Gaussian energy distribution of the laser beam changing the aperture diameter also influences the energy density in a limited range, here ±0.6 J/cm², illustrated by the dashed lines. (c) With increasing spot diameter, i.e., ablated area, the signal intensity measured on the MC-ICP-MS increases.

Reflected, transmitted and polarized light observation is available at different magnifications using exchangeable motorized objectives of 5x, 10x and 20x. Laser ablation positions can be located using high quality optical imaging via a CCD camera and stored as x, y, z coordinates in the software together with laser parameters (repetition rate, scan speed, analyses duration, washout-time between automated analyses). Before laser ablation starts, the laser focusing objective is moved into the beam path and the sample stage is automatically adjusted to the correct z-coordinate (focus length) for each individual measurements position as previously determined (autofocus or manual adjustment) and stored, to focus the laser beneath the sample surface. This setup ensures precise and reproducible laser focusing, the importance of which is discussed below. Live observation of the sample surface during laser ablation is generally impaired in image quality. Both loss of image sharpness and colour fidelity is caused by the laser focusing lens due to chromatic aberration between the UV laser light and the visible light spectrum (VIS). Our custom-designed achromatic lens-triplet partially corrects for this distortion. The remaining discrepancy in focal length between UV and VIS is compensated by a custom-built adjustable CCD camera lens tube, which allows to bring the UV laser wavelength and the visible wavelength into focus in the same plane, i.e., whilst the laser beam is focused beneath the sample surface a sharp visual image of the sample surface is obtained, allowing a better image quality during live observation of the ablation.

The energy transmission (T) of the UV laser beam through the focusing optics and the cell window was measured to be about 70%, which was found to be superior to commercially available Excimer laser optics (e.g., we tested a OFR LMU UV10x with T ≈ 50%). The pulse width of the UV wavelength after FHG conversion could not be measured directly, but was estimated to be 130 fs. This estimate is based on a pulse width measurement by autocorrelation of the residual IR pulses at the FHG output. There the IR beam has passed about 13 mm glass of optical components in transmission, resulting in 190 fs pulse width. This pulse width broadening can be used to estimate the group velocity dispersion caused by transmission through 3.5 mm of optical components in the frequency conversion beam path of the resulting FHG UV beam output. Moreover, the UV laser beam has to pass the lens-triplet for focussing and the ablation cell window to reach the sample surface. A conservative estimate for the pulse width at the sample surface therefore is <200 fs.

For laser ablation the samples are contained in a custom-designed ablation cell built at GFZ Potsdam. The cell is made of aluminium with a semi-rectangular inner chamber. The chamber can accommodate sample holders adapted for petrographic thin sections (48x55 mm) and round samples with dimensions of Ø 1/2 inch (25.4 cm) and Ø 1 inch (12.7 cm) (Fig. 1). The cell lid allows air-tight sealing and incorporates a 86 mm diameter fused silica window (2 mm thickness) with 196 nm anti-reflection coating on both sides to minimise energy loss during transmission of the laser beam (<5%). The exchangeable sample holders permit to accommodate samples of different size and shape, thereby keeping the effective free volume of the cell constant at about 18 cm³. Moreover, the insets produce a flat surface without any dead volume, which is favourable for efficient aerosol transport. The cell can be fitted with inlets and outlets of different inner diameter (ID) to influence the gas flow conditions in the cell. During this study, a He inlet nozzle with 0.5 mm ID and a He/aerosol outlet of 2.5 mm ID was used. The laser-generated aerosol is transported through a Teflon-lined Tygon tubing, 6.4 mm ID, by the He carrier gas of the ablation cell to the mass spectrometer, were it is mixed with Ar ('dry' or 'wet' as discussed below) before entering the ICP torch. At the end of each laser ablation analyses, typical wash out time of the cell and the length of the aerosol transfer tubing is less than 50 seconds, in which the signal drops to background level.

The laser spot size on the sample surface can be adjusted in two ways. First, adjusting an iris aperture in the UV beam path changes the spot size on the sample surface whilst keeping the energy density on the sample moderately constant (within +/- 25%, Fig. 2). Second, changing the vertical focus position also changes the spot size, but the energy density is modified strongly at the same time (Fig. 3).

2.3 Mass spectrometry

A *Thermo Neptune* MC-ICP-MS, equipped with a *Neptune Plus Jet Interface* (comprised of *Jet* sample cones and *Jet* interface pump *Pfeiffer OnToolBooster*) was used for isotope measurements. To resolve Si isotope signals from isobaric interferences (mainly N-O moleculars) the ion optics were operated in medium mass resolution mode (mass resolving m/Δm power at 5%, 95% intensity limits >6000). Moveable Faraday detectors with $10^{11}$ Ω amplifiers were precisely positioned to obtain interference-free flat-top peak shoulders for

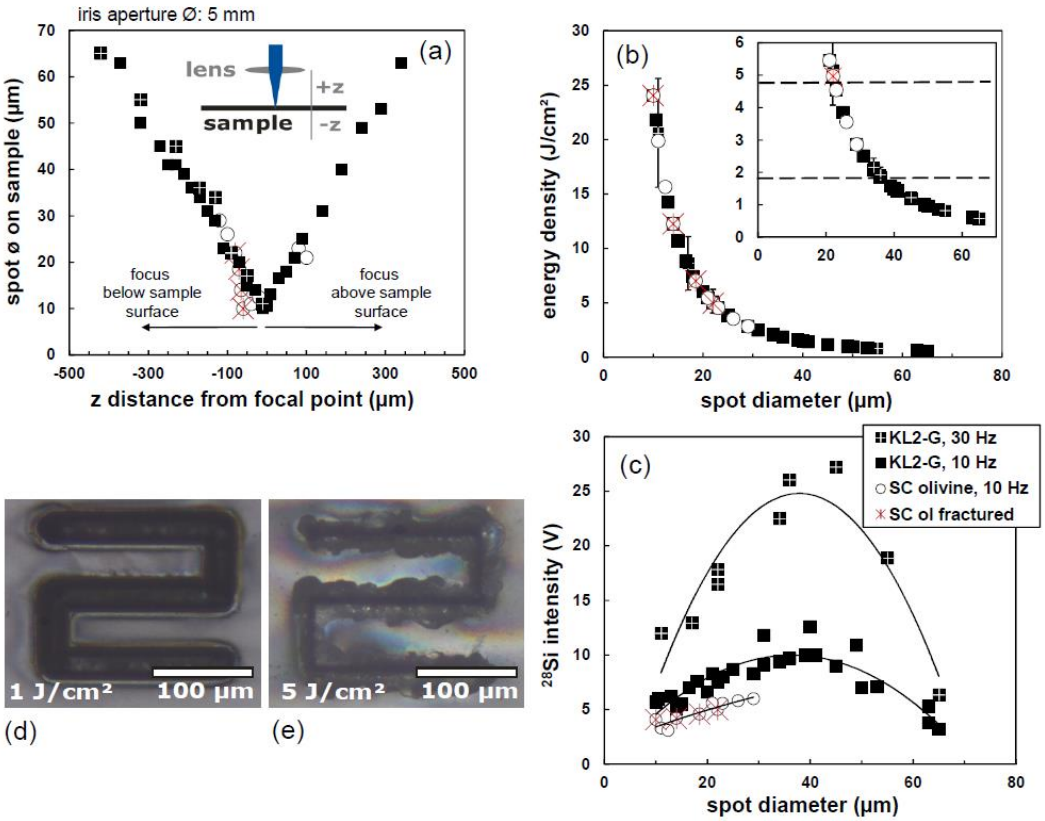


Figure 3. Influence of laser focussing on laser ablation performance. Experiments were done at both 10 Hz and [30] Hz laser repetition rate, respectively. Ion signal intensities were measured on a Faraday detector of the MC-ICP-MS. The spot diameter was systematically varied by adjusting the position of the laser focus point beneath or above the sample surface (a), resulting in changes in the calculated energy density at the sample surface (b), and signal intensity (c) during ablation on different materials. The inset in (b) shows in detail the optimum energy range (dashed lines), where a combination of laser focussing, energy density and spot size yields smooth laser ablation traces (d), without irregular ablation and fracturing of the material (e). Images (d and e) are reflected light microphotographs of laser ablation traces on olivine. Symbol in all panels are the same as explained in legend of panel (c).

simultaneous detection of all three stable Si isotopes. Faraday cups L2, C, and H2 were used for simultaneous measurements of $^{28}Si$, $^{29}Si$, and $^{30}Si$, respectively. With this cup configuration $^{27}Al$ (L4) can be detected simultaneously, which can be used for Al concentration measurements.

To independently determine the Si isotope composition of reference materials, Si was measured by solution MC-ICP-MS after sample dissolution and chromatographic purification of Si following the analytical procedure described in detail elsewhere [36, 48]. In brief, after sample decomposition of 6 to 12 mg sample powder by NaOH-fusion at 750°C in Ag crucibles for 10 minutes (using about 400 mg NaOH pellets, Merck, p. a., 1.06495.1000), samples were dissolved in Milli-Q water (18.2 MΩ) and pH was adjusted to 1.5 by HCl (dist.) addition. An aliquot of ca. 60 µg Si (in 1.8 ml) was loaded onto chromatography columns (Spectrum 104704 PP filled with 1.5 ml AG50W-X8) and Si was eluted with 5 ml $H_2O$. The Si solution was acidified to 0.1M HCl and Mg (Alfa Aesar Specpure 14430; evaporated, and dissolved in 0.1M HCl) was added to both samples and to the bracketing NBS-28 as an internal standard, to be able to use the $^{25}Mg/^{24}Mg$ ratio for mass bias drift correction between the two bracketing measurements of NBS-28; the latter being prepared by the same decomposition and Si purification procedure as the samples. Quantitative sample recovery (measured column yield >98%, i.e. complete recovery within analytical uncertainties of the concentration measurements by ICP-OES: 100 ± 5%) and purity of the Si sample solution (>97%) was checked by ICP-OES (Varian 720ES) before isotope analyses. The fusion/dissolution procedure blank contributed <0.06% of total Si, and the blank of the Si column procedure was below ICP-OES detection limit, i.e., <190 ng Si, corresponding to <0.3% of Si processed, thus being considered negligible. The analyte solutions with matched concentrations of 0.7 µg/ml of both Si and Mg (within 5%) were introduced into the MC-ICP-MS by an ESI ApexHF desolvator (sample path made of PFA) fitted with a PFA nebulizer (≈110 µl/min), thereby reaching $^{28}Si$ and $^{24}Mg$ signal intensities of >13 V and > 20 V, respectively, measured on Faraday detectors ($10^{11}$ Ω). Measurements were done in dynamic mode (magnet jump), alternating between Si and Mg isotopes for 30 cycles á 4 seconds integrations time. Based on repeat sample dissolutions and measurements, and comparison to published data on reference materials (Table 2) analytical uncertainties of solution MC-ICP-MS data are estimated to be ± 0.11‰ (2SD) and ± 0.09‰ (2SD) on $\delta^{30}Si$ and $\delta^{29}Si$, respectively. Si isotope ratios are reported in the delta notation for the $^{30}Si/^{28}Si$ ($\delta^{30}Si$) and $^{29}Si/^{28}Si$ ($\delta^{29}Si$) isotope ratios relative to NBS-28.

Operating parameters of the fsLA-MC-ICP-MS are summarised in Table 1. These represent the optimum conditions based on systematic tests. Gas flows were optimised on a daily bases but

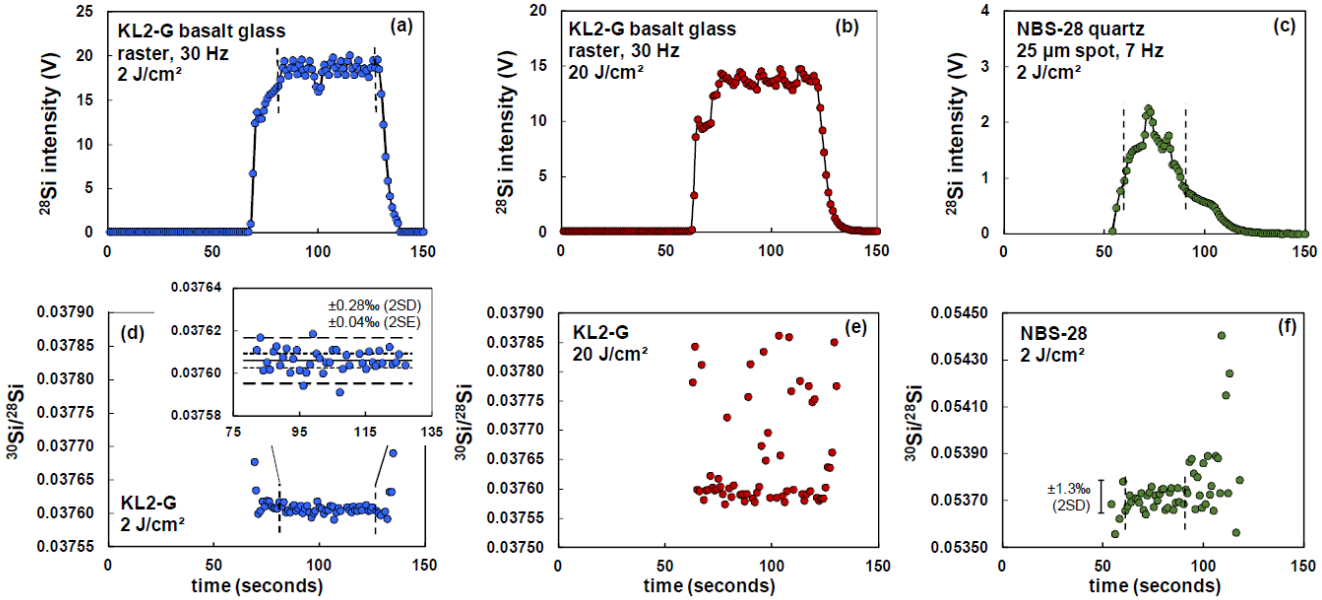


Figure 4. Signal intensities (a-c) and corresponding Si isotope ratios (d-f) as a function of time over the course of an fsLA-MC-ICP-MS measurement for raster (a, b, d, e) and single spot analyses (c, f). Each data point represents an integration time of 1 second. Vertical dashed lines indicate the data range selected for isotope ratio evaluation. The inset in (d) is a magnified view of the time-resolved $^{30}Si/^{28}Si$ ratios and their statistics given as 2 standard deviation (2SD ±0.28 ‰, dashed lines) and 2 standard error (2SE ±0.04 ‰, stippled lines) of the mean. Unfavourably high laser fluencies of 20 J/cm² (b, e) cause erratic ablation behaviour and deteriorating isotope ratio precision. During single spot analyses (c, f) the precision in the isotope ratio is limited by counting statistics due fast decreasing and overall lower $^{30}Si$ signal intensities. Intensities are decreasing as the laser ablation pit is becoming deeper and hence effective aerosol transport is reduced. The error bar in (f) represents the 2 standard deviation of the mean of isotope ratio measurements acquired within the data evaluation limits (vertical dashed lines). The 2SD of ±1.3 ‰ result in a 2SE of ±0.12 ‰.

Table 1. Optimum operating parameter of the mass spectrometer and laser ablation system for Si isotope measurements. Gas flows were tuned for optimum conditions before each measurement session together with ion-optical lenses of the mass spectrometer.

| | |
|---|---|
| **MC-ICP-MS** | *Thermo Neptune* |
| RF power | 1205 W |
| Extraction lens | -2000 V |
| Acceleration potential | -10000 V |
| Cooling gas (Ar) | 15 L $min^{-1}$ |
| Auxiliary gas (Ar) | 0.7 L $min^{-1}$ |
| Nebuliser gas (Ar) | 0.6 L $min^{-1}$ (nebulising $H_2O$ and mixing with He-LA carrier gas before introduction into the ICP) |
| LA carrier gas (He) | 1.0 L $min^{-1}$ |
| Cones | Ni: Jet sampler and H or X skimmer |
| Interface pump | Pfeiffer OnToolBooster 150 |
| | |
| **LA System** | *GFZ Fem2* (*Spectra Physics Solstice* + FHG) |
| Wavelength | 193 nm |
| Pulse width | <200 fs at sample |
| Laser energy at sample | 0.005 to 0.03 mJ; 1 to 3 J/cm² |
| Repetition rate | 2 to 100 Hz |
| Spot diameter | 20 to 40 µm |
| Scan speed | 40 µm $s^{-1}$ |
| Ablation mode | line scan/raster scan/single spot |

were close to the values reported in table 1 within 0.1 L/min. Alternative settings were tested during the optimisation process as discussed later in the text.

Previous studies have shown that wet plasma conditions can be advantageous for LA-ICP-MS by providing greater tolerance against mass load effects resulting in a higher robustness than experienced in dry plasma conditions (e.g., [49, 50]). We compared dry with wet plasma conditions, and confirmed these earlier findings. Hence, wet plasma conditions were used for all analyses and dry plasma conditions were not further explored in this study. Before entering the plasma torch, the laser-generated aerosol (He carrier gas) was mixed using a y-piece with a continuous introduction of $H_2O$ by nebulisation (using Ar as nebuliser gas) in a double pass scott/cyclonic spraychamber (SIS) with a PFA self-aspirating nebuliser at an uptake rate of about 50 µl/min. The gas flows and ion-optics of the mass spectrometer system were tuned on a daily basis during ablation on the BHVO-2G glass to achieve maximum sensitivity and stability on Si isotope signals, and to minimise intensities of molecular interferences. Typically, we observed molecular isobars for the following species, which were all resolved using the medium mass resolution slit of the Neptune: $^{16}O^{14}N^+$ <5 V (close to mass of $^{30}Si^+$), $^{14}N^{14}N^+$ <100 mV and $^{12}C^{16}N^+$ <20 mV (close to mass of $^{28}Si^+$), $^{14}N^{14}N^1H^+$ <100 mV, $^{13}C^{16}O^+$ <10 mV (close to mass of $^{29}Si^+$).

Background signal intensities were measured on-peak as gas blanks. To do so, He gas was streamed through the cell whilst the laser beam was blocked. Typically, background gas blanks

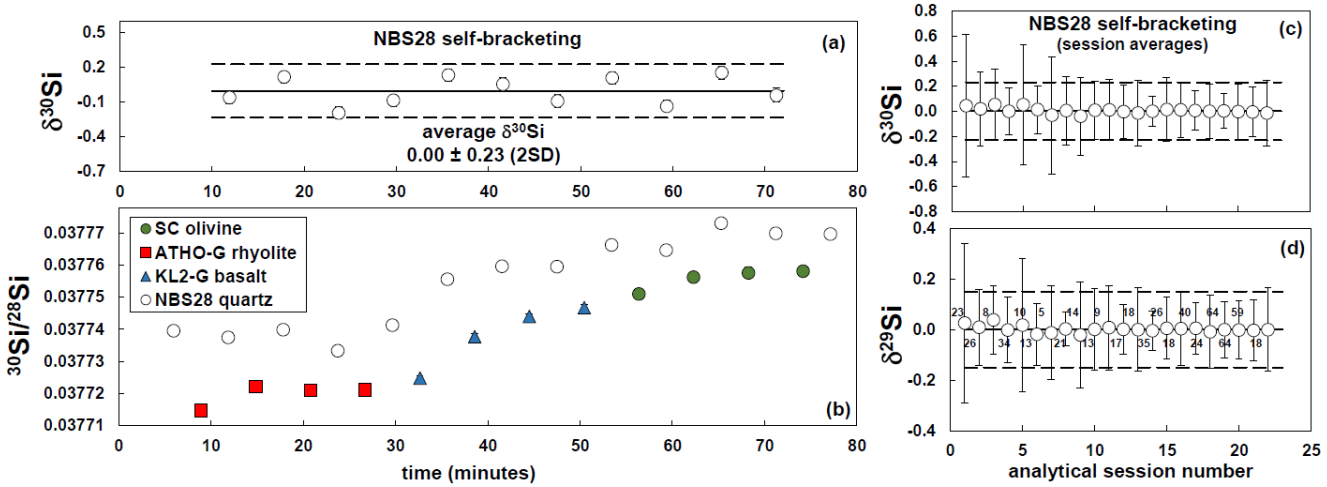


Figure 5. Illustration of mass bias stability. During isotope measurements of different samples, NBS-[28] quartz is repeatedly measured for mass bias correction, thereby bracketing each sample with two analyses of NBS-28 quartz (a, b). Signal intensities between samples and the bracketing NBS-28 were matched to within 5% by adjusting the laser repetition rate to 10, 18, 17, and 20 Hz for NBS-28, ATHO-G, KL-2G, and SC olivine, respectively. The short term stability of the instrumental mass bias (shown in panel a) allows precise isotope measurement, even if samples having different matrices are analysed subsequently (b) in the same analytical session. This NBS-28 'self-bracketing' can be used to assess the mass bias stability and therefore the overall analytical data quality for each analytical session. (c, d) δ-values for NBS-28 are session averages (n given next to each symbol in d). Before each session samples were changed in the ablation chamber, and laser and mass spectrometer operating parameters were optimised (Table 1).

(incl. $H_2O$ nebulisation) were <30 mV, <2 mV and <1 mV on $^{28}Si$, $^{29}Si$ and $^{30}Si$, respectively. The individual contributions to the total observed background signals originate from electronic noise of the detection system, impurities in gas (He, Ar) and $H^2O$-nebulisation as well as from other solid parts of the sample introduction system (e.g., tubings, torch, cones), but were not quantified separately.

The background was found to be constant and no increase with time was observed over 12 hours measurement sequences. Typical signal intensities for measurements were >7 V, >0.4 V, and >0.3 V on $^{28}Si$, $^{29}Si$ and $^{30}Si$, respectively, unless stated otherwise, and therefore background contribution to the total signal intensities were less than 0.5%.

2.4 Data acquisition and evaluation

Figure 4 shows a typical fsLA-MC-ICP-MS analysis (laser raster or spot analyses), starting with background signal measurements for 1 minute (on-peak gas blank). Each Si isotopic measurement consisted of a 5 to 10 seconds ablation stabilisation period to establish a continuous stable aerosol transport into the ICP and hence a stable Si signal, followed by 120 s of data acquisition (automatically triggered by the laser ablation system) of simultaneously detected $^{28}Si$, $^{29}Si$ and $^{30}Si$ signals ($^{27}Al$ optional). For single spot analyses shorter data acquisition times were used due to the rapidly decreasing signal as material is progressively removed and the depth of the laser ablation crater increases (Fig. 4c). Oscillations in signal intensity during raster analyses (Fig. 4a,b) are caused by slightly different ablation rates at the inflection points of the meandering laser pathway (e.g., Fig. 3d), but is not visible in the Si isotope ratios due to the static multicollection data acquisition mode. Between ablation periods the automated sample stage moved to the next measurement position, whilst the laser beam was blocked and signal intensities dropped to background levels. The time between measurements was uniformly kept at 70 seconds allowing a continuous monitoring of instrumental mass bias drift in the isotope ratio of the reference material used as measurement standard before and after each sample measurement. The standard-sample-bracketing method was used for instrumental mass bias correction by alternate fsLA measurements on samples and reference materials used as measurement standard (Fig. 5) under identical analytical conditions except for the laser repetition rate, which was adjusted to match Si intensities between samples and bracketing standards having different Si contents or different ablation behaviour. In general, NBS-28 quartz was used as measurement standard for bracketing. Other reference materials were tested, too (Table 2), as discussed below. The short-term stability of the instrumental mass bias over the time of measurements on one sample and two bracketing reference materials (Fig. 5) is better than 0.2 ‰ for the $^{30}Si/^{28}Si$ ratio, and allows precise isotope ratio measurements, even if samples having different matrices (Fig. 5) are analysed subsequently in the same analytical session.

We have compared measurements using 2 or 1 second integration times, revealing no difference in measured δ-values of reference materials and no difference in short-term repeatability of multiple analyses. Although the internal precision of individual analyses (i.e., the standard deviation (SD) of the mean of n integrations) is improving when signals are integrated over longer times, a shorter integration time has the advantage that irregularities during ablation or sample inhomogeneity can be identified more easily during data evaluation. Hence, for this study the signal intensities of all stable Si isotope were collected simultaneously with an integration time of 1 second. Each Si isotope ratio measurement comprised 80 to 120 integrations (cycles), except for single spot analyses (30 integrations).

Data evaluation was done off-line using in-house spreadsheet software and involved subtraction of the average background signal intensity (on-peak zero gas blank measured for 1 to 2 minutes at the beginning of the measurement sequence) from

each cycle before isotope ratios were computed. The mean and internal standard error of the mean at 95% confidence level (2SE = t·SD/√n; t derived from student-t distribution at 95% confidence) is calculated for each isotope ratio measurement of each sample and bracketing reference material, which are then used for calculation of δ-values and error propagation. Data quality control involved screening of the time-resolved data (e.g., Fig. 4) of each measurement for outliers using Gaussian probability density functions, temporal drift in isotope ratios during ablation (Fig. 4d, e, f) and drift between bracketing measurement standards analysed before and after each sample (Fig. 5a, b), potential spectral interferences (using the mass-dependent isotope fractionation law), and signal intensity matching between samples and bracketing standards. During each analytical session, at least one reference material having an isotope composition that was independently determined was analysed repeatedly to assess accuracy and precision. Based on the systematic tests and measurements on reference materials described in this study over the course of one year, we have defined data acceptance criteria (see section 6), which ensure a reliable and repeatable assessment of data quality for future applications of the fsLA-MC-ICP-MS method.

We have also assessed an alternative data evaluation strategy suggested by Fietzke et al. [51]. These authors extracted the average isotope ratio directly from the slope of a linear fit of the simultaneously collected signal intensities (e.g., $^{28}$Si vs. $^{30}$Si) including the signals of the background measured before and after laser ablation. We found no differences in the calculated δ-values compared to the evaluation procedure described above, except for measurements with very low signal intensities (<2 V in $^{28}$Si), where the slope evaluation method resulted in slightly better repeatability.

## 3. Results

### 3. 1 Ablation characteristics

#### 3.1.1 Laser beam profile and crater morphology

The ablation craters are morphologically characterised by the Gaussian energy distribution of the laser beam (Fig. 6a). The beam profiles of the fundamental IR wavelength and the frequency-quadrupled UV beam after transmission through the UV focussing objective (Fig. 6b), respectively, were measured using an *Ophir Spiricon* beam profiler. At 785 nm a symmetric Gaussian energy distribution is observed, whereas at 196 nm, the beam profile tends to a slightly ovoid shape, caused by the generation of the UV wavelength by overlapping the THG beam with the fundamental beam in a BBO crystal at a slightly oblique angle.

Ablation of different materials, having distinct physical properties, yields specific crater morphologies. The conical beam profile is reflected in V-shaped ablation craters in quartz (Fig. 6c, d). The Si single crystal (IRMM-017) shows numerous sharp conical spikes (Fig. 6e). Previous studies have found that the development of these spikes are controlled by the crystallographic orientation of silicon and always point along the incident direction of fs laser pulses. Their formation has been attributed to shielding of the underlying substrate by impurities on the surface, leaving the cones behind as the surrounding material is removed (e.g., [52, 53]). By repeatedly rastering the laser beam across the sample surface, the craters are incrementally deepened, eventually leading to a smooth crater surface. Ablation of dielectric materials - silicate minerals and glasses - also show a crater morphology characterised by the Gaussian laser beam profile (Fig. 6 c,d,f). However, the spikes shown on Si single crystals are absent, featuring smooth edges without visual indications of melting (Fig. 6c,d,f).

#### 3.1.2 Dependence of laser energy and beam focussing on ablation

The efficiency and rate of laser ablation is controlled by the laser fluence and is calculated according to $F = E/(\pi r^2)$, where F is the fluence [J/cm²] and E is the pulse energy [J] deposited onto the sample, with r [cm] being the crater radius measured on the sample surface. Recasting the energy delivered relative to the area illuminated provides internally consistent comparisons of the energy applied using our system. However, this approach does not take the Gaussian energy distribution of the beam into account. According to Bonse et al. [54], for a Gaussian beam the laser fluence at the cross-sectional surface with the $1/e^2$-radius $\omega_0$ can be estimated to be $F = 2E/(\pi\omega_0^2)$. Moreover, d'Abzac et al. [55] pointed out that the fluence in the focal point of the Gaussian beam can be calculated independently from measured crater diameters using the focal length of the focusing optics (f), the operating wavelength (λ), the initial diameter of the beam

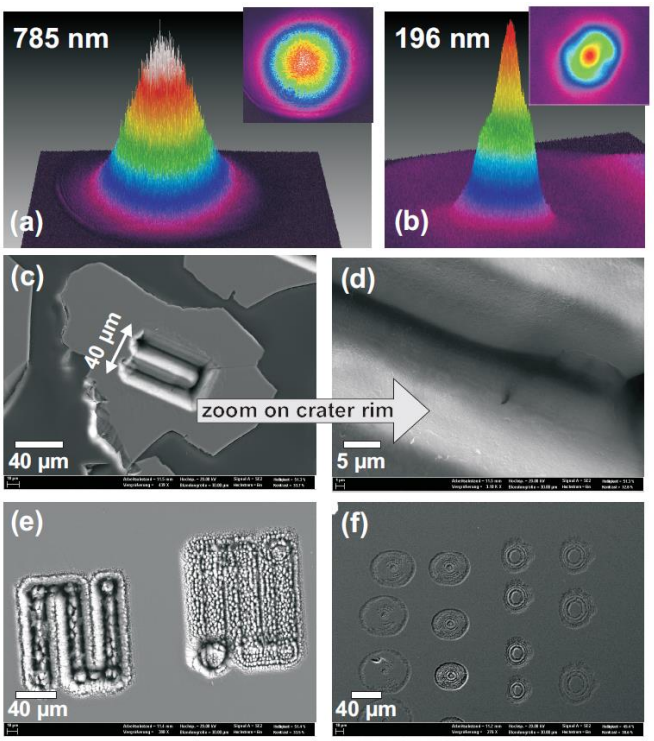


Figure 6. Laser energy beam profiles measured at (a) 785 nm and (b) 196 nm, respectively. SEM images show laser ablation traces on (c, d) quartz (NBS-$^{28}$) and (e) a silicon single crystal (IRMM-017). The raster analyses on IRMM-17 show the evolution of the laser-solid interaction during ablation, developing fewer spikes (left raster) with increasing amount of laser pulses. The spot diameter changes systematically with different z-focus position (compare Fig. 3) on BHVO-G basaltic glass (f). Spots on the right hand side of the image were generated with the laser beam focused beneath the sample surface and spots on the left hand side with a focus point above the sample surface.

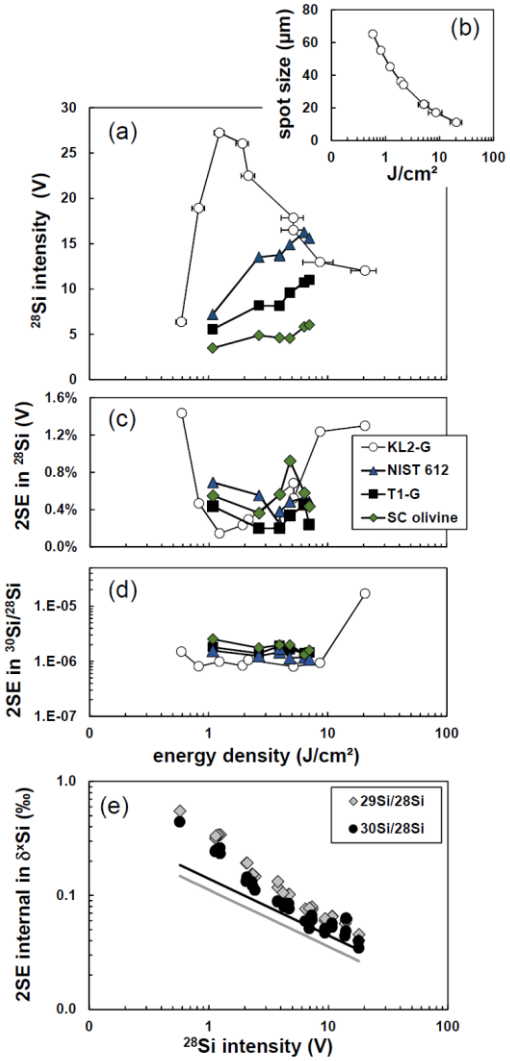


Figure 7. The influence of laser energy density on signal intensity (a) and precision in the Si intensity (c) and Si isotope ratios (d), respectively, are shown for two different experiments during fsLA of four different materials (KL2-G and T1-G glasses, NIST 612 soda-lime glass, SC olivine crystal) at a laser repetition rate of 30 Hz. In the first experiment (closed symbols), the energy density on the sample was varied by adjusting the laser output power between 3 and 22 mW, whilst keeping the laser focussing and spot diameter constant (20 µm spot Ø). In the second experiment (open symbols) the laser focus position beneath the sample surface was systematically varied to produce a larger range in energy densities (resulting in different laser spot diameters on the sample surface, as shown in b), whilst keeping the laser output energy constant. Panel (e) illustrates the influence of counting statistics on the precision in δ-values for the $^{29}Si/^{28}Si$ and $^{30}Si/^{28}Si$ isotope ratios (combined 2SE uncertainty computed by error propagation of the individual statistical uncertainties, i.e., 2 standard error of the mean from 80 to 90 integrations (at 1 s each), of one sample measurement and two bracketing reference material (RM) measurements). Each bracketing sequence was measured at different signal intensities, whilst keeping the intensities of sample and bracketing RM matched. The solid lines represent the degradation of the precision theoretically predicted from counting statistics (√n), i.e. following a slope of -0.5 in a logarithmic plot.

before passing the focusing optics (D) and the pulse energy (E) according to $F = E/(\pi\Phi^2/4)$, with $\Phi = 2.43\cdot(\lambda f)/D$. However, we prefer not to use this approach, as in our setup the laser beam is defocused and the focal point is beneath the sample surface. During the ablation process the crater deepens. Ablation typically progresses less than 20 µm over an ablation period of about 2 minutes. This depth is much less than the approx. 150 µm at which the focal point is positioned beneath the sample surface to obtain a spot diameter between 30 and 40 µm (see next paragraph). Hence, the energy density interacting with the sample surface does not reach the high values present in the focal point. Fluence values reported in this study have therefore to be considered as minimum values.

It was found that the focussing and hence the fluence of the laser beam had an effect on the ablation behaviour, depending on the nature of the analysed material. A basaltic glass (KL-2G) and an olivine crystal (SC olivine) were ablated using different fluencies (Fig. 3), which were varied by changing the focus position of the laser beam relative to the sample surface, thereby resulting in a variable ablation spot size on the sample surface (Fig. 3a-c). It was found that focussing the laser beam very close to the surface of the sample at energy densities above about 5 J/cm² resulted in irregular ablation of olivine, characterised by fracturing of the surface and chipping off of large crystal fragments (Fig. 3e). Keeping the energy density below 5 J/cm² by defocussing the laser beam (i.e., moving the focus point further beneath the sample surface) avoided this fracturing. Such irregular ablation is disadvantageous for LA-ICP-MS as it deteriorates the spatial resolution by collateral damage and reduces the efficiency of the fs-LA-MC-ICP-MS measurements because large particles are not transported by the carrier gas to the ICP. Moreover, a large particle size distribution ejected from the samples and transported by the gas stream might lead to incomplete ionisation in the ICP source of the mass spectrometer, leading to a laser-induced bias of the measured isotope ratio [15, 25, 56]. Irregular ablation was not detected on silicate glasses using light microscopic observation - even at a fluence >20 J/cm². The difference in ablation behaviour might originate in the physical properties of the samples. The investigated SC olivine crystal was formed under high temperature and pressure conditions in the upper mantle [57, 58] before being transported to the Earth's surface and therefore probably accumulated considerable strain in the crystal structure, whereas the amorphous silicate glass synthesised at atmospheric pressure lacks such structural strain and hence reacts less violent during interaction with the laser beam.

From figure 3c, we can identify an optimum range in the signal intensity vs. spot size space to obtain the highest laser ablation efficiency. By adjusting the focus position to >150 µm beneath the surface results in a surface spot diameter between 30 and 40 µm. At a fixed laser energy of about 0.015 mJ at the sample surface, the resulting energy density is between 1 and 2 J/cm², and the signal intensity on $^{28}Si$ measured on the MC-ICP-MS reaches a maximum (Fig. 3c). Further increase in spot diameter does not result in a higher signal intensity because the defocused cross section of the Gaussian laser energy distribution projected onto the sample surface results in a lower average fluence and less efficient ablation within the irradiated area. As the exact way in which the fluence is computed is not always reported, we are not always able to compare these energy densities to those reported in other studies using lasers with Gaussian beam profiles (e.g., fs-Ti:Sa or ns-Nd-YAG).

To investigate the effect of laser energy density (fluence) on signal intensity and isotope ratio precision at a constant spot size, systematic measurements were made on four different materials (NIST612, T1-G, KL-2G, SC olivine) (Fig. 7). By adjusting the output power of the pump laser in the regenerative amplifier (and optimising the amplifier to attain lowest pulse widths) fluencies can be varied from about 1 to 7 J/cm², thereby maintaining a measured energy stability of better than 3%. In this case the spot diameter on the sample surface is held constant at 20 µm (closed symbols in Fig. 7 a,c,d). All measurements were performed at a laser repetition rate of 30 Hz showing an increasing trend of the measured $^{28}$Si intensity with increasing laser fluence (Fig. 7a). However, the signal increase is most pronounced (by up to 50% relative) when fluence is increased from <1 to 2.4 J/cm². The signal increases less strongly when the laser fluence is further increased up to 7 J/cm². In this fluence range the signal intensity gain is less than 20% when laser energy is increased by 65%. The range of the applied fluence was extended above 7 J/cm² by adjusting the focus position as discussed above, thereby changing the spot diameter on the sample surface as well (Fig. 6b). Therefore, the trends above 7 J/cm² shown in figures 6a-c (open symbols) do not only represent a change in fluence but a combined effect of varying fluence and varying area irradiated by the laser.

For isotope ratio measurements it is desirable to achieve signals of such high intensity that good counting statistics by the ion detection system are achieved. It is furthermore desirable to maintain stable signals over the duration of the measurement, so that the deteriorating effect on precision caused by transient signals, which fluctuate faster than the response time of the Faraday amplifiers, is minimised [59]. The dependence of the uncertainty (expressed as the internal standard error of the mean of 60 isotope ratio measurements acquired during 1 minute of laser ablation) on the measured Si signal intensity (Fig. 7c) and Si isotope ratio (Fig. 7d) on the laser energy shows that the most precise measurements are obtained in the intermediate range of tested energy densities (1 to 4 J/cm²), where signal intensities are high enough to obtain good counting statistics. Stable ablation conditions are thus achieved at relatively low laser fluence, consistent with the observation of irregular ablation of olivine at high laser fluence. Close inspection of the time-resolved isotope ratios acquired over about one minute of ablation on basaltic glass KL2-G shows that at high fluence (≈ 20 J/cm², Fig. 4e) the precision in the $^{30}$Si/$^{28}$Si ratio is deteriorated compared to measurements at lower fluence (≈ 2 J/cm², Fig. 4d). Similar observations were made during fsLA-MC-ICP-MS Si isotope measurements on the Si single crystal reference material IRMM-017 [25].

### 3.2 Optimising ion intensity/background ratios and counting statistics

Ultimately, the precision of isotope ratio measurements is limited by counting statistical limitations of the Faraday detection system. These limits we estimate first. In the subsequent sections we then evaluate other sources of error and bias, such as sample aerosol production by laser ablation, transport of aerosol into the ICP source of the mass spectrometer as well as from fractionation in the ICP source/interface (instrumental mass bias).

The uncertainty contribution originating from counting statistics of a measured signal can be calculated from the standard deviation of a Poisson distribution (√n, where n = number of counted ions). The average voltage measured during each laser ablation measurement was converted into the number of ions counted per second (cps) by applying a conversion factor of $6.24 \cdot 10^7$ cps $V^{-1}$ for $10^{11}$ Ω (R) resistors in the amplifier. For signal intensities in the range from about 0.9 V for $^{28}$Si (i.e., about 0.05 V and 0.03 V for $^{29}$Si and $^{30}$Si, respectively) to 19 Volts for $^{28}$Si (i.e., 1.0 and 0.7 V for $^{29}$Si and $^{30}$Si, respectively) the counting-statistical uncertainty in $\delta^{30}$Si and $\delta^{29}$Si values were calculated (Fig. 7e). This calculation includes uncertainty contributions from three independent isotope ratio measurements, i.e. one sample measurement and two bracketing measurements on a reference material, which were combined into a total uncertainty for each δ-value using error propagation.

These computed definitional uncertainties can be compared to the uncertainties of actual laser ablation Si isotope measurements. The latter were calculated as standard errors of the mean at 95% confidence ($2SE = t \cdot 2SD/\sqrt{n}$) of 80 to 90 integrations (n) during each laser ablation period. For these measurements the ion beam intensities were varied by adjusting the laser repetition rate. Fig. 7e shows a decrease in the uncertainty of Si isotope ratios with increasing ion beam intensity measured at the Faraday detector. We also observe a discrepancy between the measured and the predicted counting statistical uncertainties, becoming more prominent at low ion beam intensities. At signal intensities >7 V on $^{28}$Si, the observed uncertainty is getting close to the predicted counting statistical uncertainty. Any remaining difference to the theoretically predicted uncertainty from counting statistics is likely attributed to uncertainty contributions from mass bias instabilities in the ICP source (plasma flicker and drift), aerosol production by laser ablation as well as amplifier response time and Johnson noise of the detector system. We did not quantify the individual uncertainty contributions but we can qualitatively assess from Figure 7e that at low signal intensities besides counting statistics other sources of uncertainty become more and more prominent. Hence, for precise Si isotope ratio measurements signal intensities >7 V on $^{28}$Si are desirable.

Note that for these measurements ion beam intensities were corrected for a background contribution by means of an on-peak zero measurement (see section 2.3). At background/signal ratios of less than 0.5 %, that are achieved at sample signal intensities of >7 V on $^{28}$Si this blank-subtraction results in $\delta^{29}$Si or $\delta^{30}$Si values, respectively, that are within 0.03 ‰ to the uncorrected $\delta^{29}$Si or $\delta^{30}$Si. Hence, the background contribution is negligible. At lower ion beam intensities, however, background corrections can be more substantial, and can reach up to 0.13 ‰ in δ-values at background/signal ratios of 2%. Still, to minimise this correction, maintaining the ion beam intensities above 7 V on $^{28}$Si is adapted wherever possible in this study. Such intensities are typically attainable at an ablated surface area of > 50x50 µm, obtained by rastering the defocused laser beam along the sample surface.

### 3.3 Dependence of the accuracy on mass load effects and sample/standard signal intensity matching

The presence of different amounts of sample in the ICP might lead to a bias in the measured isotope ratio caused by changes in instrumental mass bias [50, 60]. However, it is desirable to apply the standard-sample-bracketing technique using reference materials as measurement standards that may have different Si concentrations than samples. This approach would lead to highly variable ion beam intensities depending on the Si content of

Table 2. Si isotope data analysed by fsLA-MC-ICP-MS (this study), solution MC-ICP-MS (this study) after chromatographic separation of Si, and average values compiled from the literature.

| | | fsLA-MC-ICP-MS (this study) | | | | | | | | solution MC-ICP-MS (this study) | | | | | published (average values) | | | | |
|---|---|---|---|---|---|---|---|---|---|---|---|---|---|---|---|---|---|---|---|
| sample | | $\delta^{29}Si/^{28}Si_{NBS28}$ (‰) | 2SD[b] | $\delta^{30}Si/^{28}Si_{NBS28}$ (‰) | 2SD[b] | n | rep rate (Hz) | ablated area[d] | bracketing RM[f] | $\delta^{29}Si/^{28}Si_{NBS28}$ (‰) | 2SD[b] | $\delta^{30}Si/^{28}Si_{NBS28}$ (‰) | 2SD[b] | n | $\delta^{29}Si/^{28}Si_{NBS28}$ (‰) | 2SD | $\delta^{30}Si/^{28}Si_{NBS28}$ (‰) | 2SD | references[e] |
| IRMM-017 | Si single crystal | -0.69 | 0.11 | -1.31 | 0.11 | 5 | 7 | R 50x50 µm | NBS28 | -0.71 | 0.09 | -1.36 | 0.10 | 4 | -0.68 | 0.09 | -1.32 | 0.13 | [25*, 26, 27, 36] |
| | | -0.60 | 0.15 | -1.17 | 0.19 | 6 | 7 - 30 | L 35x65 µm | NBS28 | | | | | | | | | | |
| | | -0.63 | 0.15 | -1.22 | 0.24 | 32 | 7 | R 65(100)x100 µm | NBS28 | | | | | | | | | | |
| | ***mean*** | ***-0.63*** | ***0.15*** | ***-1.22*** | ***0.23*** | ***43*** | | | | | | | | | | | | | |
| | | -0.59 | 0.64 | -1.40 | 0.52 | 4 | 2 | S 25 µm | NBS28 | | | | | | | | | | |
| BHVO-1 | basalt | | | | | | | | | -0.15 | 0.07 | -0.27 | 0.10 | 4 | -0.16 | 0.02 | -0.30 | 0.05 | [30, 31, 38, 48, 65] |
| BHVO-2[a] | basalt glass (fused powder) | -0.16 | 0.09 | -0.36 | 0.18 | 12 | 16 | R 100x100 µm | BHVO-2G | -0.15 | 0.04 | -0.27 | 0.11 | 4 | -0.16 | 0.05 | -0.29 | 0.05 | [28, 29, 32, 33*, |
| BHVO-2G | basalt glass | -0.17 | 0.12 | -0.36 | 0.19 | 46 | 20-35 | R 100x100 µm | NBS28 | | | | | | | | | | 36, 37, 65] |
| | | -0.17 | 0.19 | -0.39 | 0.26 | 5 | 100 | R 100x100 µm | IRMM-017 | | | | | | | | | | |
| | | -0.21 | 0.14 | -0.39 | 0.22 | 16 | 18-35 | R 100x100 µm | NIST612 | | | | | | | | | | |
| | | -0.12 | 0.11 | -0.24 | 0.18 | 4 | 18-35 | R 100x100 µm | JER | | | | | | | | | | |
| | ***mean*** | ***-0.17*** | ***0.13*** | ***-0.36*** | ***0.20*** | ***83*** | | | | | | | | | | | | | |
| | | -0.07 | 0.66 | -0.06 | 0.61 | 4 | 7 | S 25 µm | IRMM-017 | | | | | | | | | | |
| JER | diopside glass | 0.00 | 0.13 | 0.03 | 0.22 | 4 | 20 | R 100x100 µm | IRMM-017 | -0.06 | 0.09 | -0.15 | 0.10 | 8[c] | -0.04 | 0.14 | 0.02 | 0.32 | [25*] |
| SC olivine | olivine (San Carlos) | -0.14 | 0.20 | -0.24 | 0.28 | 7 | 10 | R 100x100 µm | NBS28 | | | | | | -0.20 | 0.10 | -0.34 | 0.15 | [12*, 12, 38] |
| | | | | | | | | | | | | | | | -0.41 | 0.11 | -0.81 | 0.19 | [25*] |
| ATHO-G | rhyolite glass | -0.21 | 0.10 | -0.38 | 0.20 | 14 | 20-40 | R 100x100 µm | NBS28 | -0.11 | 0.02 | -0.19 | 0.07 | 4 | -0.28 | 0.11 | -0.60 | 0.21 | [22*] |
| | | -0.19 | 0.11 | -0.39 | 0.17 | 8 | 30-40 | R 100x100 µm | NIST612 | | | | | | | | | | |
| | ***mean*** | ***-0.21*** | ***0.10*** | ***-0.38*** | ***0.18*** | ***22*** | | | | | | | | | | | | | |
| ML3B-G | andesite glass | -0.24 | 0.20 | -0.48 | 0.32 | 6 | 20 | R 100x100 µm | BHVO-2G | -0.15 | 0.01 | -0.28 | 0.11 | 4[c] | -0.16 | 0.11 | -0.35 | 0.20 | [24*] |
| T1-G | diorite glass | | | | | | | | | -0.09 | 0.05 | -0.22 | 0.08 | 5[c] | -0.13 | 0.11 | -0.23 | 0.20 | [24*] |
| KL2-G | basalt glass | -0.22 | 0.18 | -0.36 | 0.23 | 6 | 17 - 37 | R 100x100 µm | NBS28 | -0.14 | 0.06 | -0.28 | 0.11 | 10[c] | -0.21 | 0.11 | -0.44 | 0.20 | [24*, 33*] |
| NIST 612 | silicate glass | -0.05 | 0.13 | -0.07 | 0.15 | 5 | 30 - 35 | R 100x100 µm | NIST612 | 0.01 | 0.09 | 0.02 | 0.12 | 4 | | | | | |
| | | 0.02 | 0.10 | 0.03 | 0.21 | 15 | 30 - 35 | R 100x100 µm | NBS28 | | | | | | | | | | |
| NIST 610 | silicate glass | -0.02 | 0.17 | -0.03 | 0.31 | 5 | 35 | R 100x100 µm | NIST612 | | | | | | | | | | |
| NBS28 | quartz | 0.09 | 0.24 | -0.09 | 0.55 | 5 | 7 | S 25 µm | NBS28 | | | | | | ≡ 0 | | ≡ 0 | | |

a fsLA-MC-ICP-MS measurements of BHVO-2 were done on glass, prepared by flux-free fusion of powders (Ir strip heater), whereas BHVO-2G is already supplied as glass by USGS.

b Repeatablity reported as 2 standard deviation of the mean of n analysis. Uncertainty (long term repeatability) of the fsLA-MC-ICP-MS method is estimated to be ±0.15 ‰ (2SD) and ±0.23 ‰ (2SD) for $\delta^{29}Si$ and $\delta^{30}Si$, respectively. Uncertainty of the solution MC-ICP-MS method is estimated to be ±0.09 ‰ (2SD) and ±0.11 ‰ (2SD) for $\delta^{29}Si$ and $\delta^{30}Si$, respectively (for details see text).

c Replicate analysis (n) on two independent dissolutions by NaOH fusion and subsequent chromatographic Si purification.

d Ablated area refers to raster (R), line scans (L) and single spot (S) analyses.

e Average of published values compiled from bulk solution isotope analyses of the materials, except for *, which were obtained by LA-MC-ICP-MS.

f Indicated is the reference material (RM) used as a measurement standard for calibration (mass bias correction) during fsLA-MC-ICP-MS analyses. All delta values are reported relative to NBS-28; when other reference materials (RM) were used as bracketing RM , the results where recalculated to the NBS-28 scale using the average published value or the solution MC-ICP-MS data obtained in this study, where no published data was available.

various materials. However, we aim to keep the ion beam intensities of Si isotopes of the sample identical to that of the reference material. Such intensity matching is important to minimise differences introduced between sample and standard from tailing of interference peaks close to the Si masses. The latter issue can be improved by optimised tuning of Ar and He gas flows to minimise N-O moleculars and by subtraction of on-peak background signals. However, contribution of the background correction to the uncertainty budget of the isotope ratio should best be minimised. Hence, intensity matching between sample and bracketing measurement standard is desirable. To achieve this intensity matching we adjusted the repetition rate of the laser (Fig. 8), whilst introducing differences in mass load of elements other than Si between the standard and the sample.

We employed two different strategies to investigate the effect of such differences in total ICP mass load and relative sample/standard signal intensity matching on the accuracy of Si isotope measurements. In the first strategy laser ablation was performed with a variety of repetition rates and therefore variable mass transfer per time into the plasma, whilst keeping the Si signal intensities of sample (BHVO-2G, IRMM-017, NBS-28) and bracketing reference material (NBS-28) closely matched (Fig. 8a,b). No systematic bias in the measured $\delta^{30}$Si values outside of the uncertainty limits of the method (Fig. 8a, b) was detectable. This result validates our approach to use NBS-28 as bracketing measurement standard for isotope analyses of materials having different Si concentrations.

In the second strategy, laser repetition rates were also varied for the 'unknown samples', but the repetition rate of the bracketing measurement standard was kept constant (Fig. 9). In this setup we used NIST612 for both 'unknown sample' and 'bracketing standard'. Hence the 'true' $\delta^{30}$Si of NIST612 is 0‰, and any deviation from 0‰ outside of the analytical uncertainty limits is readily apparent. The results of this experiment disclose how close the signal intensities between sample and bracketing standard need to be matched to obtain accurate results (Fig. 9a).

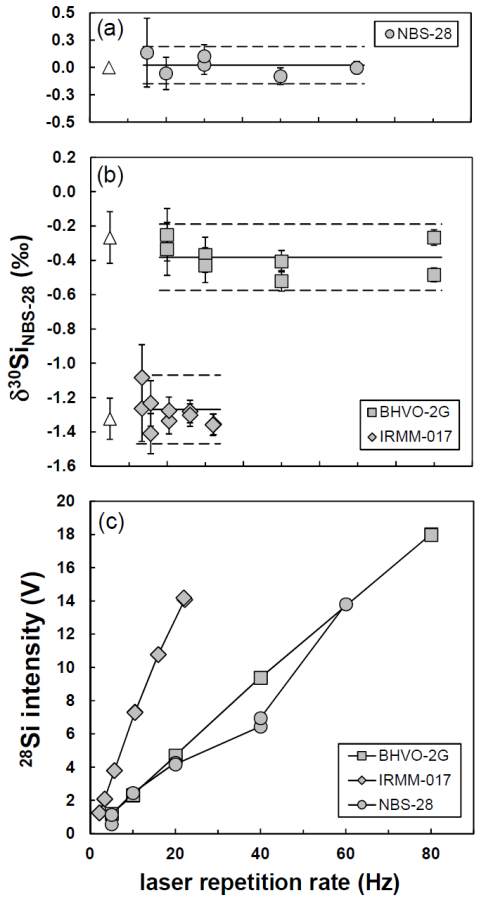


Figure 8. Systematic tests for mass load effects during fsLA-MC-ICP-MS Si isotope analyses on different materials (BHVO-2G basaltic glass, IRMM-17 Si single crystal, NBS-$^{28}$ quartz). (a, b, c) Mass load in the ICP was varied by adjusting the laser repetition rate, which resulted in increased ablation rate and hence increasing Si signal intensity (c) with increasing repetition rate. Each $\delta^{30}$Si value (a, b) is obtained from a sample measurement bracketed by two NBS-$^{28}$ measurements, where the intensity during sample ablation was matched to the intensity of the bracketing standards to within 10% (the x-axis of the diagrams shows the repetition rate employed for the samples). Open triangles represent the average $\delta^{30}$Si values of each reference material taken from the literature (Table 2).

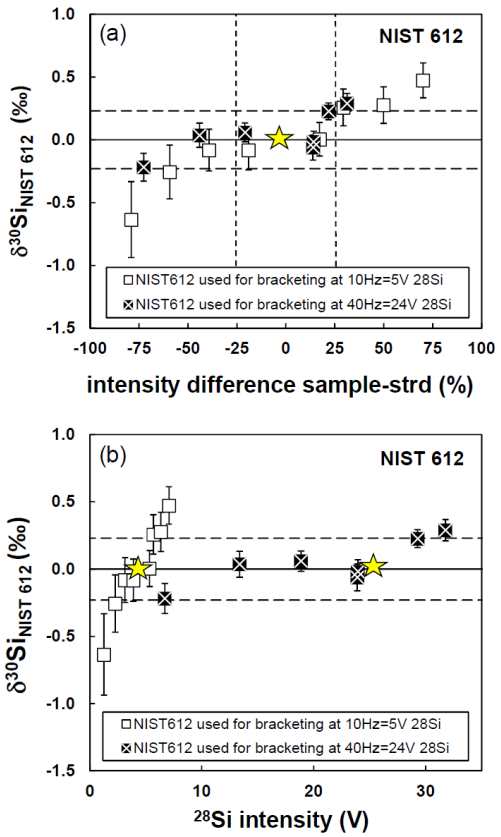


Figure 9. Effect of intensity mismatch between samples and intermittent bracketing standards plotted against a) % intensity difference; b) measured intensity. $\delta^{30}$Si measurements were made using NIST 612 as both 'unknown sample' and bracketing reference material, i.e. here the true $\delta^{30}$Si of NIST 612 is 0 ‰ (star in panel a). The repetition rate, and hence ICP mass load, was changed for each 'sample' ablation (NIST 612), but kept constant at 10 Hz and 40 Hz, respectively, for the bracketing standard (NIST 612); indicted by the stars. The vertical dashed lines in panel (a) indicate the allowed range in intensity. Even though the on-peak background signal was subtracted from the raw data, some minor tailing of molecular interferences close to the Si masses might affect measurements at low Si intensities.

Here, we tested a relative intensity difference between sample and bracketing reference materials ranging from -75% to +75%. It is evident that intensity matching is required to within 25% to obtain $\delta^{30}$Si values that are accurate to within 0.2‰. If the Si signal intensity of the sample differs from that of the bracketing measurement standard by more than 75%, for example, a systematic bias of up to 0.6 ‰ in $\delta^{30}$Si can occur. This effect is more pronounced at overall lower Si signal intensities (e.g., 5 V on $^{28}$Si, Fig. 9) as compared to higher Si signal intensities (e.g., 24 V on $^{28}$Si, Fig. 9). The difference occurs because at lower signal intensities the signal/background ratio becomes unfavourably low – in particular for the less abundant isotope – and the background contribution, which affects both

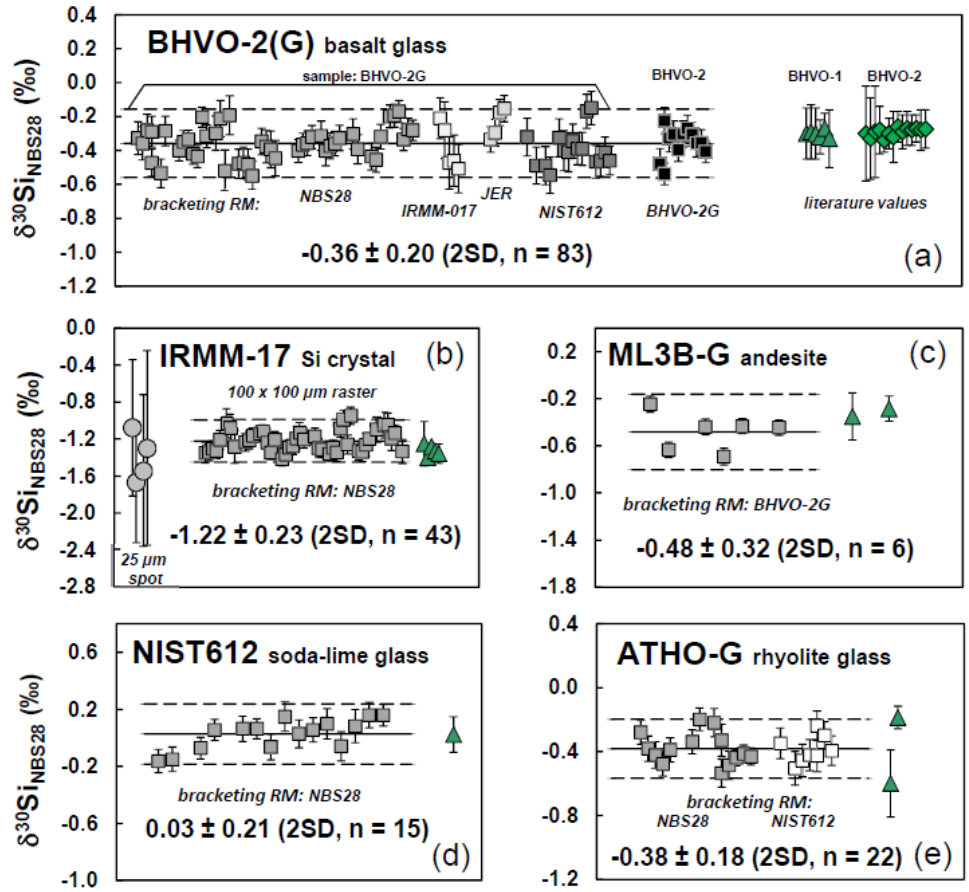


Figure 10. Replicate fsLA-MC-ICP-MS analyses of silicon isotope compositions for different materials, using different reference materials (RM) for calibration by standard-sample-bracketing. Squares denote raster analyses, circles are single spot analyses (see Table 2). Within uncertainties the results agree with reference values (green triangles and diamonds. Horizontal dashed lines represent the long-term analytical uncertainty of the fsLA-MC-ICP-MS method (±0.23 ‰, 2SD).

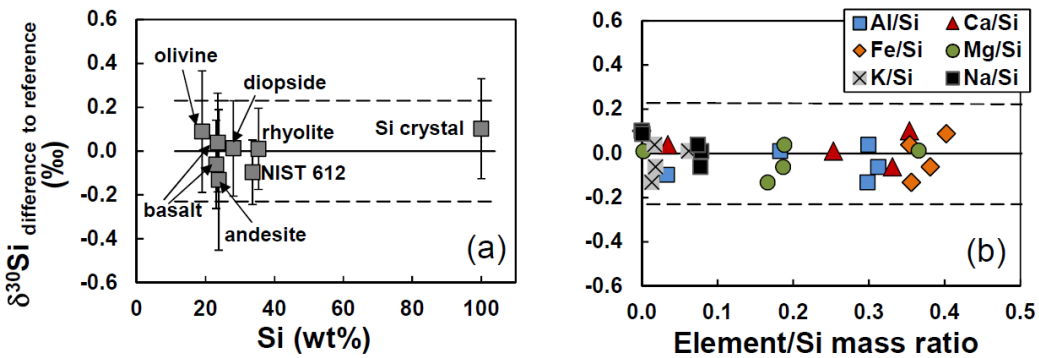


Figure 11. Shown are deviations of average $\delta^{30}$Si values obtained by fsLA-MC-ICP-MS to independently determined reference values as a function of Si concentration (a) and Element/Si ratios (b), illustrating the wide range in chemical composition. Various bracketing reference materials were used for calibration (compare Table 2). The agreement between the fsLA data and the reference data within uncertainties (horizontal dashed lines), shows absence of any composition-dependent matrix effects during non-matrix-matched standard-sample-bracketing analyses of Si isotopes by fsLA-MC-ICP-MS.

measurements on sample and bracketing reference material, does not cancel out. Moreover, the uncertainty in the background measurement (at very low signal intensities close to the detection limit) increases through the increased on-peak background correction and limits imposed by counting statistics (compare error bars in Fig. 9b, which are 2SE internal standard error of the mean of individual LA analyses). Consistent with our results, other studies using LA-MC-ICP-MS, e.g., [15, 25, 61], and solution MC-ICP-MS, e.g., [62, 63], also indicate that signal intensity matching is improving accuracy. Hence, we conclude that Si signal intensity matching should be within 25%, achieved by individually adjusting the laser repetition rate for measurements on samples and bracketing reference materials.

3.4 Investigation of matrix effects

Matrix effects can be caused by spectral interferences on the Si isotope masses or by non-spectral changes in instrumental mass bias. As mentioned above, observed interferences caused by molecules entrained in the ICP from the atmosphere, where they are ionised ($^{16}O^{14}N^+$, $^{14}N^{14}N^+$, $^{12}N^{16}N^+$, $^{16}O^{14}N^+$, $^{12}C^{16}O^+$) were resolved in medium mass resolution mode of the Neptune mass spectrometer. Potential interferences from doubly charged species related to elements contained in the samples are $^{56}Fe^{++}$ ($m/z \approx 28$), $^{58}Ni^{++}$ and $58Fe^{++}$ ($m/z \approx 29$), and $60Ni^{++}$ ($m/z \approx 30$), which are not resolved at the mass resolution of our measurements. The presence of interferences becomes evident as deviations from the mass-dependent fractionation law in a three isotope plot (e.g., Appendix A, Fig. A1). Mathematically, the presence of interferences can be rapidly detected by a deviation from the mass dependent relation ($\Delta^{29}Si' = \delta^{30}Si - 1.93 \times \delta^{29}Si \equiv 0$). We did not detect deviations outside the analytical uncertainties, even for the iron-rich basaltic samples. Hence, in subsequent analyses sequences we used the $\Delta^{29}Si'$ as data quality control, i.e., accepted deviations from zero must be within analytical uncertainties, which was typically <0.1 ‰, as observed from numerous measurements on Fe and Ni free reference materials (Table 2).

Non-spectral matrix effects are important to consider in Si isotope measurements. Using the standard-sample-bracketing method these effects occur when the measurement standard used for calibration of the isotope ratio measurements of unknown samples does not behave identical as the sample. The resulting effects are often referred to as laser-induced and ICP-induced matrix effect, respectively (e.g., [15, 64]). Causes of such matrix-effects are non-stoichiometric ablation, incomplete vaporization/ionisation of large particles in the ICP, or a variable space charge effect in the mass spectrometers' ICP interface. Differences in the chemical and physical properties between samples and reference materials used for calibration can therefore potentially affect the accuracy of the measured isotope compositions.

We have systematically tested for such matrix-effects by using different reference materials for calibration, which were analysed directly before and after each material measured as 'unknowns'. The results are given in Table 2 and illustrated in Fig. 10.

First, we observe that all $\delta^{30}Si$ values of the different materials analysed by fsLA-MC-ICP-MS agree within uncertainties with $\delta^{30}Si$ of currently available reference values (Fig. 10). One exception is SC olivine. Our data, $\delta^{30}Si = -0.24 \pm 0.28$ ‰ (2SD), is in good agreement with data obtained from a range of different olivines from the San Carlos suite with $\delta^{30}Si$ values ranging from -0.27 to -0.45 ‰, averaging $-0.34 \pm 0.15$ ‰ (2SD) [12, 39]. This range also covers data obtained on olivines from a wide range of igneous rocks (see review by [65]). However, the $\delta^{30}Si$ value of $-0.81 \pm 0.19$ ‰ (2SD) reported in a previous fsLA-MC-ICP-MS study [25] is outside this range.

Second, we observe that accurate values were obtained regardless of the reference material used for bracketing (Fig. 10), despite the markedly different physical and chemical properties. The diversity in chemical composition can be seen in figure 11, revealing no systematic dependence of $\delta^{30}Si$ values on the Si content and Element/Si ratios of the analysed materials. Again, this finding confirms that one single reference material can be used for calibration (ideally NBS-28, which is the international 'δ-zero' reference material) for a wide range of different materials.

3.5 Precision, accuracy, spatial resolution, and material consumption

The conditions favouring precise and accurate Si isotope measurements, such as optimised laser focussing and energy density resulting in regular ablation and continuous production of sample aerosol over the time of the measurements, as well as high signal intensities for good counting statistics, correlate inversely with spatial resolution. When smaller volumes are ablated, less material is supplied to the ICP source of the mass spectrometer within shorter timescales. We explored various spatial scales, ranging from single spot analyses (spot Ø >25 µm) to raster or line scan analyses, where the laser bean was scanned across the sample surface along line paths or rectangular areas.

Comparison of the data obtained from measurements at different spatial resolutions shows that an ablated surface area of ≥50x50 µm (raster analysis), or line scans covering an equivalent area, at crater depths <20 µm result in isotope ratio data with the lowest uncertainties (Table 2). From this volume (between $10 \cdot 10^3$ to $50 \cdot 10^3$ µm³) sufficient material is ablated to obtain constant and high ion signals on all Si isotopes over the analyses time of at least one minute (e.g., Fig 4a). However, at a spatial resolution of about 25 µm, i.e. during single spot analysis, the signal intensities are lower and are decreasing fast (Fig. 4c), leading to an inferior uncertainty in the isotope ratio data (Fig. 4f, Table 2). Several studies involving transient signal processing have shown that isotope ratios derived from rapidly rising or decreasing signals can be affected by delayed Faraday amplifier response times (e.g., [51, 59, 66, 67]). The decreased precision of the spot analysis shown in Figure 4f might contain a contribution of this effect. Yet, a trend resulting from differential amplifier response time is not discernible as the scatter of individual ratio measurements overwhelms this effect which would in any case be cancelled out by standard-sample bracketing. To summarise, the nature of the scientific question hence requires evaluation of a trade-off between precision and spatial resolution.

The use of the *Jet interface* of the *Neptune* mass spectrometer enhanced sensitivity, so that lower laser repetition rates can be used. The total sample material consumption required for precise isotope ratio measurements is thus between $10 \cdot 10^3$ to $50 \cdot 10^3$ µm³, which corresponds to <15 ng Si for an analysis of quartz. A rough guideline is that 10 ng is consumed for materials containing 100 wt% Si, and 60 ng for materials containing 20 wt% Si.

Comparison to previous laser ablation Si isotope studies shows that for the same level of precision in $\delta^{30}$Si more than $30 \cdot 10^3$ µm³ (≈ 50 ng Si) was consumed [25]. However, using the same method described in Chmeleff et al. [25], that was modified by using x skimmer cones, Steinhoefel et al. [33] report an enhancement in sensitivity. For published nsLA-MC-ICP-MS methods minimum sample consumption is estimated to be between $160 \cdot 10^3$ µm³ (equivalent to ≈ 200 ng Si for quartz) [68] to $40 \cdot 10^3$ µm³ (equivalent to ≈ 55 ng Si for quartz) [12]. For comparison, the lower depth penetration (a few µm at most) of the SIMS methods can achieve a much lower total volume consumption (< $1 \cdot 10^3$ µm³) for a Si isotope ratio measurement. Using spot diameters of 10 to 20 µm, $\delta^{30}$Si values have been determined with an uncertainty of about ±0.5 ‰ (2SD) [16, 17]. Careful matrix-matching of the measurement standard or empirically determined composition-dependent matrix corrections was employed in these SIMS measurements, however.

To evaluate the performance, the measurement uncertainty is a key analytical parameter. Measurement uncertainty comprises components from systematic errors (bias) including contributions from corrections and assigned δ-values of reference materials used for calibration, as well as contributions from random effects, which can be described by statistics [69, 70]. We evaluated the uncertainty of the method based on analyses of various reference materials over multiple analytical sessions over the course of one year and compared these results to independently obtained reference values. The long term repeatability on the two most frequently analysed reference materials, IRMM-017 (n = 43) and BHVO-2 (n = 83), indicates an uncertainty estimate of the fsLA-MC-ICP-MS method of ±0.23 ‰ (2SD) and ±0.15 ‰ (2SD) for $\delta^{30}$Si and $\delta^{29}$Si, respectively. Comparison of the fsLA-MC-ICP-MS data obtained in this study with reference values (Table 2) indicates that results are also accurate within uncertainties. This uncertainty estimate compares well to the repeatability of NBS-28, which was regularly measured as bracketing measurement standard in between different samples in 22 separate analytical sessions (Fig 5c,d), and resulted in a dataset of 603 individual NBS-28 isotope ratio measurements. When treating every second NBS-28 analysis as an 'unknown' and using the bracketing NBS-28 analyses for mass bias correction (here called NBS-28 'self-bracketing'), the repeatability of NBS-28 can be obtained for each analytical session (Fig. 5c,d), which was on average ±0.26 ‰ (2SD) and ±0.15 ‰ (2SD) for $\delta^{30}$Si and $\delta^{29}$Si, respectively. This uncertainty estimate does not include the single spot analyses at 25 µm spatial resolution, which resulted in a somewhat inferior uncertainty, estimated to be ±0.6 ‰ (2SD) for $\delta^{30}$Si. We also note that internal errors (2SE) of single analysis might underestimate the uncertainty in δ-values, but are valuable statistical parameters for assessment of the individual analytical data quality or for relative comparison of spot-to-spot-variability in the isotope composition within the same sample, when analysed during the same analytical session. Hence, we conclude that the uncertainty of the fsLA-MC-ICP-MS method is ±0.23 ‰ (2SD) for $\delta^{30}$Si and ±0.15 ‰ (2SD) for $\delta^{29}$Si, and these should be applied to data for geological interpretation and comparison to results obtained in other laboratories.

## 4. Discussion

That a single, non-matrix-matched reference material can be used for calibration for a large variety of sample materials without inducing matrix effects is in agreement with previous studies. Several studies reported that laser-induced matrix effects are significantly reduced during fsLA as compared to nsLA, rendering the need for rare matrix-matched reference materials unnecessary. For example, successful non-matrix matched Fe and Si stable isotope measurements by fsLA-MC-ICP-MS was reported (e.g., [15, 61, 71, 72]). In contrast, other workers reported systematic offsets during fsLA-MC-ICP-MS measurements of Cu isotopes [73]. We note that some nanosecond LA-MC-ICP-MS studies reported non-matrix-matched calibration of B stable isotope measurements, [74-77], whereas others circumvented this problem by employing matrix-matched reference materials for Li, Mg, Si, Fe and Sr stable isotope [12, 51, 68, 78-82] measurements. Here, we focus on the effects found in femtosecond laser ablation.

To shed light onto the apparently disparate results reported for some fsLA-MC-ICP-MS measurements, we discuss first laser-induced matrix effects. Laser-induced matrix effects arise when the samples differ from the reference materials used for calibration not only in terms of chemical composition but also in their physical properties. In laser ablation, the thermal conductivity is an important parameter. Thermal effects during laser ablation can lead to melting of the sample, potentially leading to non-stoichiometric sampling. The fs laser ablation process (multi-photon absorption, e.g., [15, 83]) occurs on timescales short enough to minimise transfer of thermal energy from the electron level to the phonon level – as opposed to ns laser ablation. Therefore, if the thermal conductivity of samples and reference material used for calibration are comparable, laser-induced bias is potentially minimised, in particular for nsLA. However, if materials with very high thermal conductivity are ablated, even fsLA might be affected by thermal ablation effects. This hypothesis is supported by the observation that accurate isotope data was obtained when samples and reference materials for calibration had similar thermal conductivity (e.g., when samples and calibrators are both dielectrics, such as silicates), despite differences in chemical composition (e.g., [12, 76, 80]). On the other hand, when thermal conductivity between sample and calibrator was very distinct, e.g., Cu metal (≈ 400 W/m/K, [84]) vs. sulphides (< 40 W/m/K, [84]) or Fe metal (≈ 80 W/m/K, [84]) vs. silicates (< 7 W/m/K, [84]), a bias in the measured δ-values was observed for fsLA [12] and nsLA [73], respectively.

A second form of mass discrimination might be introduced during aerosol transport. It has been shown that fs laser ablation produces different types of particles (agglomerates and spheres) that can have different aerodynamic size and variable isotopic composition [85-87]. A matrix effect arises if these particles are discriminated against each other [85-87]. Our systematic investigation of the influence of laser energy density on the precision and accuracy of Si isotope ratios (see section 3.1.2) indeed suggests that generation of large particles by a focused laser beam at high laser fluence has negative effects on the precision of isotope ratio measurements (Fig. 4e). This deterioration might be due to insufficient transport capabilities of the He gas flow or by incomplete ionisation of large particles in the ICP [15, 25]. Hence, we recommend employing a defocused laser beam, thereby limiting the laser fluence to less than 3.8 J/cm² on the sample surface. Under these optimised conditions, we have no indication that isotope ratio measurements are biased due to aerodynamic size discrimination (Fig. 4d) and that the laser-generated aerosol is transported without bias to the ICP.

A third discrimination effect might arise in the ICP. For materials on which femtosecond lasers reduce the matrix effects caused by the ablation process itself, matrix effects are instead induced in the ICP. A first important difference in the mode of operation of the fsLA-MC-ICP-MS set-up in this study is the use of wet plasma conditions. Even with signal intensity matching, mass load effects might potentially affect the accuracy of isotope measurements. The continuous introduction of water into the plasma seems to support more robust conditions. Indeed, under wet plasma conditions, a variable mass load from the laser aerosol revealed no mass load effects (Fig. 8). Previous studies that have successfully performed non-matrix-matched fsLA-MC-ICP-MS for Fe and Si isotope analyses [15, 25, 33, 61, 71] all employed wet plasma conditions (G. Steinhoefel, pers. commun.). In contrast Ikehata et al. [73] showed the need for matrix-matched reference materials for calibration to obtain accurate Cu isotope measurement on sulphides under dry plasma conditions; although we have to note that it is not possible to discern the potential effects of laser-induced and ICP-induced effects in the study of Ikehata et al., where only dry plasma conditions were employed.

Hence, for accurate stable isotope measurements the combination of a defocused femtosecond laser beam, to reduce thermal laser-induced matrix effects, with robust wet plasma conditions, to reduce ICP-induced matrix effects (e.g., [15]), seems to be a favourable combination.

## 5. Application: Si isotope weathering signals at the micro scale

Previous studies have shown that silicon isotopes can be used as a tracer of weathering processes (e.g., review by [88] and references therein). Isotope fractionation takes place during biogeochemical reactions in the Critical Zone at the Earth's surface, such as secondary mineral formation or utilization of silicon in the biosphere. During chemical weathering, precipitation of secondary phases from aqueous solutions can be associated with equilibrium isotope fractionation but also with kinetic isotope fractionation, where the lighter isotopes react more readily, thereby enriching the solid reaction product in lighter isotopes. After isotopically light Si was removed a complementary fluid reservoir remains that must be isotopically heavy.

We have applied the fsLA-MC-ICP-MS method to investigate the Si isotope signatures of weathering in a corestone in the beautiful tropical, humid, and mountainous highlands of Sri Lanka. The corestone was taken from the base of a highly weathered 10 m deep regolith profile developed from a charnockite bedrock lithology, which major mineralogy consists of K-feldspar (32 vol%), quartz (30 vol%), plagioclase (25 vol%), biotite (7 vol%) and orthopyroxene (4 vol%). Further details on sampling location and mineralogical and chemical compositions are described elsewhere [44]. The corestone is characterised by spheroidal weathering, i.e. a concentric advance of the alteration front from the surface towards the centre of a corestone, which produced several zones, progressing from the centre to the rim (Fig. 12a): an unweathered centre (zone 1), a light grey part (zone 2), the yellow-brownish colored part (zone 3) and the surrounding rindlets (zone 4). In the study of Hewawasam et al. [44] pyroxene and plagioclase were identified as the first minerals affected by alteration, whereas K-feldspar, quartz and biotite do not show significant dissolution features. Therefore, abundant plagioclase is the predominant source of Si during weathering and we have focused the Si isotope study on plagioclase and its secondary weathering products in the corestone zone 4 (Fig. 12a ), where secondary minerals formed during weathering are enriched in Al, Si and Fe comprising mainly of kaolinite, goethite, and gibbsite, as well as their amorphous precursor phases [44]. We have analysed the Si isotope composition of plagioclase as well as of secondary weathering products in the cavities and in grain boundaries between weathered plagioclase crystals (Fig. 12b). For plagioclase

Table 3. Si isotope data obtained by fsLA-MC-ICP-MS on the Hakgala corestone

| sample analysis number[a] | $\delta^{29}Si/^{28}Si_{NBS28}$ (‰) | 2SE[b] | $\delta^{30}Si/^{28}Si_{NBS28}$ (‰) | 2SE[b] | fsLA parameter[c] |
|---|---|---|---|---|---|
| *Plagioclase, Corestone Zone 4* | | | | | |
| HakCore5-pl-01 | -0.13 | 0.06 | -0.28 | 0.06 | (1) |
| HakCore5-pl-02 | -0.04 | 0.06 | -0.19 | 0.08 | (1) |
| HakCore5-pl-03 | -0.10 | 0.06 | -0.28 | 0.07 | (1) |
| HakCore5-pl-04 | -0.14 | 0.06 | -0.30 | 0.06 | (1) |
| HakCore5-pl-05 | -0.08 | 0.07 | -0.30 | 0.07 | (1) |
| HakCore5-pl-06 | -0.16 | 0.06 | -0.25 | 0.07 | (1) |
| HakCore5-pl-07 | -0.11 | 0.05 | -0.07 | 0.06 | (1) |
| HakCore5-pl-08 | -0.09 | 0.05 | -0.12 | 0.07 | (1) |
| HakCore5-pl-09 | -0.09 | 0.06 | -0.16 | 0.08 | (1) |
| HakCore5-pl-10 | -0.10 | 0.07 | -0.07 | 0.08 | (1) |
| HakCore5-pl-11 | -0.17 | 0.06 | -0.30 | 0.09 | (2) |
| HakCore5-pl-12 | -0.07 | 0.05 | -0.13 | 0.09 | (2) |
| HakCore5-pl-13 | -0.19 | 0.05 | -0.35 | 0.09 | (2) |
| HakCore5-pl-14 | -0.19 | 0.06 | -0.34 | 0.09 | (2) |
| *Plagioclase, Corestone Zone 1* | | | | | |
| HakCore2-pl-01 | -0.14 | 0.08 | -0.25 | 0.10 | (1) |
| HakCore2-pl-02 | -0.12 | 0.08 | -0.17 | 0.10 | (1) |
| *average plagioclase (Zone 1 and 4, n = 16)* | | | | | |
| **mean** | **-0.12** | | **-0.22** | | |
| **2SD** | **0.09** | | **0.19** | | |
| *Secondary Weathering Products, Corestone Zone 4* | | | | | |
| HakCore5-sec-01 | -0.30 | 0.11 | -0.72 | 0.16 | (3) |
| HakCore5-sec-02 | -0.29 | 0.10 | -0.63 | 0.16 | (3) |
| HakCore5-sec-03 | -0.41 | 0.08 | -0.82 | 0.12 | (3) |
| HakCore5-sec-04 | -0.55 | 0.11 | -1.13 | 0.18 | (3) |
| HakCore5-sec-05 | -0.50 | 0.11 | -0.95 | 0.19 | (3) |
| HakCore5-sec-06 | -0.23 | 0.09 | -0.44 | 0.15 | (3) |
| HakCore5-sec-07 | -0.18 | 0.08 | -0.24 | 0.12 | (3) |
| HakCore5-sec-08 | -0.31 | 0.11 | -0.72 | 0.17 | (3) |
| HakCore5b-sec-09 | -0.24 | 0.10 | -0.48 | 0.12 | (4) |
| HakCore5b-sec-10 | -0.18 | 0.09 | -0.27 | 0.17 | (4) |
| HakCore5b-sec-11 | -0.22 | 0.06 | -0.56 | 0.08 | (4) |
| HakCore5b-sec-12 | -0.37 | 0.10 | -0.75 | 0.15 | (4) |
| HakCore5b-sec-13 | -0.20 | 0.14 | -0.49 | 0.18 | (4) |
| HakCore5b-sec-14 | -0.54 | 0.12 | -1.09 | 0.19 | (4) |
| HakCore5b-sec-15 | -0.14 | 0.06 | -0.25 | 0.09 | (4) |
| HakCore5b-sec-16 | -0.30 | 0.06 | -0.48 | 0.09 | (4) |
| HakCore5b-sec-17 | -0.25 | 0.08 | -0.63 | 0.11 | (4) |
| HakCore5b-sec-18 | -0.22 | 0.05 | -0.51 | 0.08 | (4) |
| HakCore5b-sec-19 | -0.33 | 0.06 | -0.74 | 0.10 | (4) |
| HakCore5b-sec-20 | -0.60 | 0.07 | -1.12 | 0.10 | (4) |
| HakCore5b-sec-21 | -0.34 | 0.06 | -0.71 | 0.10 | (4) |
| HakCore5b-sec-22 | -0.58 | 0.06 | -1.24 | 0.11 | (4) |

[a] HakCore5 and HakCore5b represent two different thin sections, prepared from the same zone of the corestone by wet (5) and dry (5b) grinding/polishing techniques, respectively.

[b] 2SE is the internal standard error of the mean (95% confidence, t $SD/n^{0.5}$) for individual fsLA analysis, propagated from the counting statistics of the sample and the two bracketing NBS-28 measurements (each with n = 60 integrations). Uncertainty (long term repeatability) of the fsLA-MC-ICP-MS method is estimated to be ±0.15 ‰ (2SD) and ±0.23 ‰ (2SD) for $\delta^{29}Si$ and $\delta^{30}Si$, respectively, which should be applied for geological interpretation.

[c] Laser ablation parameter: (1) spot Ø30 µm, 100 x100 µm raster, 20 Hz, 1 J/cm²; (2) spot Ø20 µm, 80 x100 µm raster, 30 Hz, 3.5 J/cm²; (3) spot Ø30 µm, line scan, 25 Hz, 1 J/cm²; (4) spot Ø20 µm, line scan, 15 Hz, 3.5 J/cm². All fsLA-MC-ICP-MS analyses were done using NBS28 quartz as bracketing measurement standard.

analyses, the laser ablation locations were carefully chosen on fresh, unaltered parts of the crystals, previously identified using light microscopy and scanning electron microscopy observations. For comparison, we also measured plagioclase crystals from the unweathered zone 1 of the corestone (Fig. 12a).

In addition to the data quality control described in the text, we also tested potential influence of ablation of small proportions of epoxy resin during fsLA-MC- ICP-MS analyses, which was used to prepare the thin sections and might be present in the cavities, where secondary weathering products were analysed. This experiment involved Si isotope analyses on the JER diopside glass, which was mounted into the same epoxy resin as the corestone sample. To simulate the effect of partial epoxy ablation the laser beam was rastered over the surface of the diopside glass directly at the contact to the surrounding epoxy resin, where the ablated area covered both ablation on diopside glass and epoxy resin (see Appendix A, Fig. A2). For Si isotope measurements, the standard-sample-bracketing method was used, where each glass + epoxy analysis was bracketed by a laser ablation measurement of the same diopside glass located in the centre of the glass fragment. For comparison, pure diopside glass was also measured as an unknown. The results for glass + epoxy measurements ($\delta^{30}Si$ = 0.09 ± 0.14 ‰, 2SD, n = 7) are identical to the measurements on pure diopside glass ($\delta^{30}Si$ = 0.00 ± 0.08 ‰, 2SD, n = 6) and therefore indicate that partial ablation of epoxy resin does not introduce a bias in $\delta^{30}Si$ (Fig. A2). We note that the internal uncertainty in δ–values for individual analyses tends to be slightly larger for glass + epoxy analyses compared to pure glass analyses (Appendix A, Fig. A2), which is also observed in the corestone dataset (Table 3). Furthermore, we also tested any effect introduced by the thin section preparation procedure (wet or dry) and found no difference (Table 3).

The results of Si isotope measurements in the corestone are shown in figure 12c and listed in table 3. Plagioclase $\delta^{30}Si$ values comprise a narrow range and no differences between zone 1 and zone 4 can be found. The mean $\delta^{30}Si$ from 16 individual plagioclase grains is -0.22 ± 0.19 ‰ (2SD), identical to the mean $\delta^{30}Si$ of the upper continental crust (-0.25 ± 0.16 ‰ [32]). The secondary weathering products cover a range in $\delta^{30}Si$ from -0.24 ‰ to -1.24 ‰. These ratios are consistently lower as compared to the Si source signature (plagioclase). Isotopically light Si of secondary phases, relative to the bedrock source, is consistent with findings of Si isotope studies at the soil scale, which found that bulk soils rich in secondary minerals as well as mineral-specific extractions (leaching of amorphous and poorly crystalline phases) are isotopically lighter ($\delta^{30}Si$ = -2.95 ‰ to -0.16 ‰) than the parent silicate material (see [88] and references therein). Consistent with this observation made at the micro scale are isotopically heavy Si signatures of dissolved Si in rivers, representing the complementary reservoir (see [88] and references therein). Hence, processes operating at the micro scale can be traced to the river scale. Strikingly, the data obtained in this study covers a large range in $\delta^{30}Si$ of secondary weathering products, highlighting the advantage of in-situ isotope measurements. Here, processes at the micro scale become visible, which are not resolved by mineral-specific extractions using different chemical reagents that integrate the Si isotope signal on the bulk sample scale.

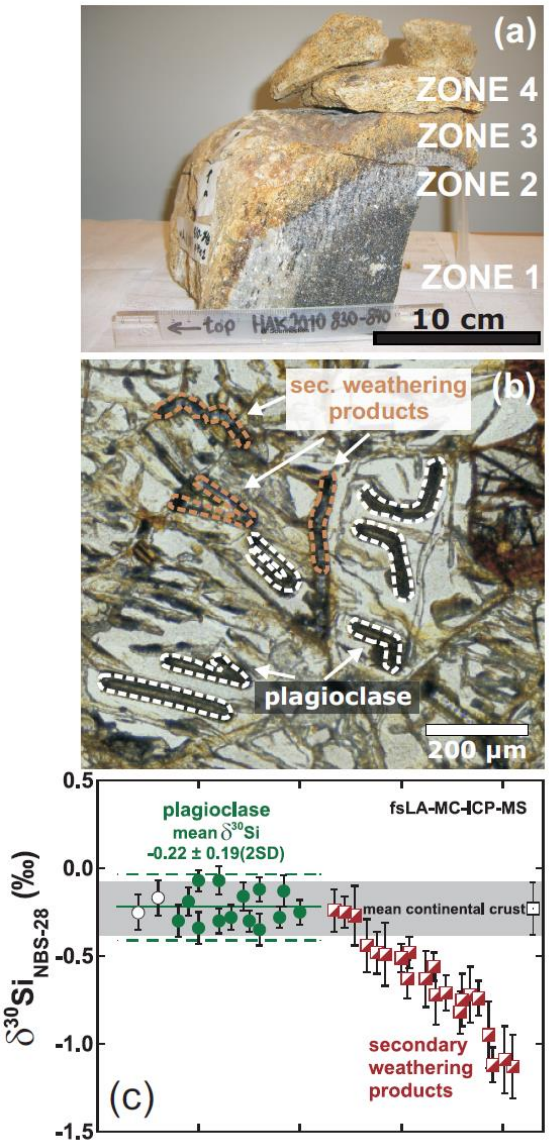


Figure 12. A corestone from a regolith profile in Sri Lanka (a) was analysed for Si isotopes by fsLA-MC-ICP-MS in plagioclase and secondary weathering products (b). (c) The results show that unweathered plagioclase from zone 1 (open circles) and zone 4 (close circles) of the corestone is identical in $\delta^{30}Si$ to the mean upper continental crust (open square and horizontal grey bar [32]). Secondary weathering products formed between weathered plagioclase crystals. These are isotopically light in $\delta^{30}Si$.

## 6. Conclusions

We presented the technical specifications of a new in-house built femtosecond laser ablation system coupled to a MC-ICP-MS. We evaluated the analytical conditions for optimum parameters of in-situ analyses of Si stable isotope ratios in a variety of geological materials at the 0.2 ‰ level (2SD). By testing the limits of the method it is possible to define quality control and data acceptance/rejection criteria. These can be transferred to future applications of the method, and to other elements. The fsLA-MC-ICP-MS technique was applied to characterise the Si

isotope composition of international reference materials and to the study of rock weathering processes at the micro scale.

Based on the evaluation of analytical conditions in this study a protocol is summarised for quality control and to identify and avoid analytically dubious data. This protocol involves data rejection/acceptance criteria, that were selected to achieve analytical conditions required to attain precise and accurate Si isotope data at the 0.2 ‰ level.

1. Before samples with previously untested matrix types are analysed, the absence of matrix effect needs to be verified by analysis of a reference material with a matrix as similar as possible in terms of chemical and physical properties. Such a homogeneous reference material should be measured by both fsLA-MC-ICP-MS and solution MC-ICP-MS after chromatographic separation of Si to verify that results agree within uncertainty limits.

2. Si isotope data of unknown samples are accepted only if at least one reference material of 'known' Si isotope composition is repeatedly analysed in the same analysis session and is within the general uncertainty limits of the independently determined reference value.

3. Signal intensities of the samples are matched to within ± 25% to the bracketing reference material used for calibration by adjusting the laser repetition rates. Signal intensities should ideally not fall below 7 V (on a $10^{11}$ Ω resistor) in $^{28}$Si to attain precise Si isotope data at the 0.2 ‰ level (2SD).

4. Si isotope data of natural, terrestrial samples have to follow the mass-dependent fractionation law within their uncertainty limits, typically $\Delta^{29}Si' = \delta^{30}Si - 1.93 \times \delta^{29}Si = 0 \pm 0.1$ ‰. Otherwise they are rejected as analytical outliers.

5. Each analysis consisting of at least 30 Si isotope ratio measurements (i.e., 30 integrations) is screened for robust analytical conditions. In particular, a normal distribution of the data population is verified. Then, as laser ablation paths are located on two-dimensional sample surfaces, tapping of other phases having distinct isotope ratios can be identified in the time-resolved data as the ablation progresses into depth of the samples. Moreover, outliers can be identified in the time-resolved data caused by irregular ablation or fluctuations in the plasma source of the MS.

6. To avoid irregular ablation, the energy density should be adapted to the physical properties of the ablated materials, ideally between 1 and 3 J/cm².

7. Sample measurements for which the two bracketing standard measurements exceed an instrumental mass bias drift of 0.3 ‰ in the $^{30}$Si/$^{28}$Si ratio or which are subject to short term erratic deviation from the general trend in mass bias drift, are rejected.

*Acknowledgements*
K.P. Jochum (MPI Mainz, Germany) is thanked for providing the BHVO-2 glasses, prepared by flux-free melting in an Ir-strip heater. M. Oelze, M. Tatzel, H. H. Schopka and G. Steinhoefel are acknowledged for support and discussion on chemical separation of Si and (LA) Si isotope mass spectrometry. T. Hewawasam, J. L. Dixon and J. Bouchez are thanked for sampling the core stone in the field. The authors are also indebted to the aforementioned and to R. Behrens for discussion on the Sri Lanka core stone. W. Steiner and his GFZ workshop team are credited for support in construction of the laser ablation cell. J. Buhk is thanked for technical support in the fsLA-MC-ICP-MS laboratory. I. Schaepan is acknowledged for assistance with scanning electron microscope imaging of laser ablation craters. This manuscript benefited from the valuable input of two anonymous reviewers.

Appendix A

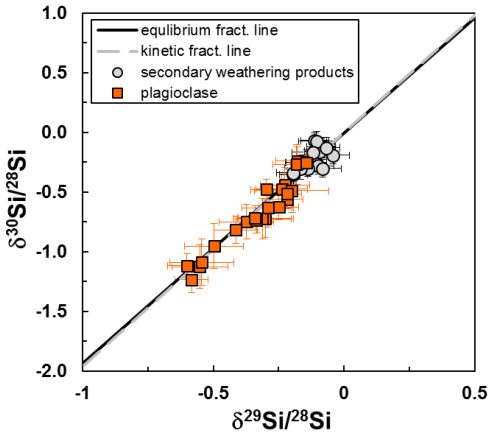


Figure A1. Three-isotope-plot of corestone Si isotope data. Lines represent mass-dependent fractionation lines with a slope of 1.93 (equilibrium law) and 1.96 (kinetic law).

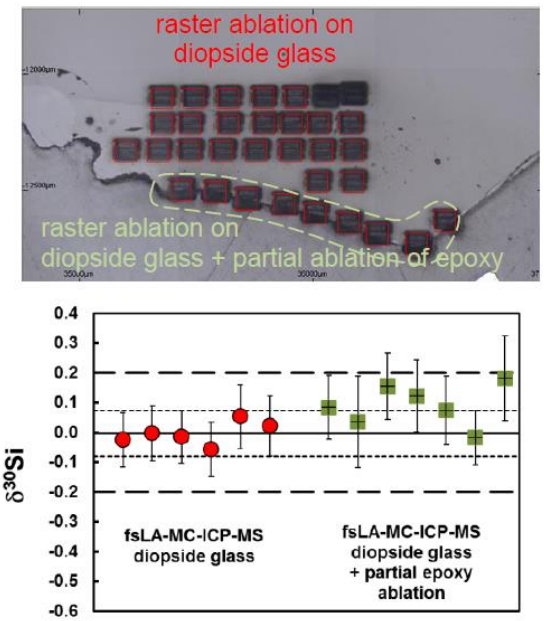


Figure A2. Testing the influence of partial epoxy ablation. Si isotope data obtained by fsLA-MC-ICP-MS on JER diopside glass (circles) and on diospide glass with partial ablation of epoxy resin (see microphotograph for locations). The data was obtained by a 100 x 100 µm raster analyses at 20 Hz laser repetition rate, using the same diopside glass as bracketing standard throughout. Hence, the $\delta^{30}$Si of the diopside glass ≡ 0‰. The horizontal lines represent the mean (solid line) and 2SD of the repeat analyses (stippled lines) on JER diopside glass. The dashed lines represent the uncertainty (long-term repeatability) of the fs-LA-MC-ICP-MS method, as determined by replicate

analyses of reference materials (see text and Table 2). The results show that ablation of epoxy resin does not introduce a systematic bias during fsLA-MC-ICP-MS analyses of Si isotopes as both 'pure diopside' data ($\delta^{30}Si = 0.00 \pm 0.08$ ‰, 2SD, n = 6) and 'diopside+epoxy' data ($\delta^{30}Si = 0.09 \pm 0.14$ ‰, 2SD, n = 7) are identical within uncertainties. However, it has to be noted that the internal standard error of the mean (2SE) for each measurement is slightly larger in the case of epoxy ablation, probably due to larger signal intensity variations.

## References


[1] E.H. Evans, J.J. Giglio, Interferences in inductively coupled plasma mass spectrometry. A review, Journal of Analytical Atomic Spectrometry, 8 (1993) 1-18.

[2] E.H. Evans, J.B. Dawson, A. Fisher, S.J. Hill, W.J. Price, C.M.M. Smith, K.L. Sutton, J.F. Tyson, Atomic Spectrometry Update. Advances in atomic emission, absorption, and fluorescence spectrometry, and related techniques, Journal of Analytical Atomic Spectrometry, 16 (2001) 672-711.

[3] E.H. Evans, C.D. Palmer, C.M.M. Smith, Atomic spectrometry update. Advances in atomic spectrometry and related techniques, Journal of Analytical Atomic Spectrometry, 27 (2012) 909-927.

[4] M.W. Loewen, A.J.R. Kent, Sources of elemental fractionation and uncertainty during the analysis of semi-volatile metals in silicate glasses using LA-ICP-MS, Journal of Analytical Atomic Spectrometry, 27 (2012) 1502-1508.

[5] D. Gunther, S.E. Jackson, H.P. Longerich, Laser ablation and arc/spark solid sample introduction into inductively coupled plasma mass spectrometers, Spectrochimica Acta Part B-Atomic Spectroscopy, 54 (1999) 381-409.

[6] B.J. Fryer, S.E. Jackson, H.P. Longerich, Design, operation and role of the laser-ablation microprobe coupled with an inductively-coupled plasma-mass-spectrometer (LAM-ICP-MS) in the earth sciences, Canadian Mineralogist, 33 (1995) $^{30}$3-312

[7] S.F. Durrant, Laser ablation inductively coupled plasma mass spectrometry: achievements, problems, prospects, Journal of Analytical Atomic Spectrometry, 14 (1999) 1385-1403.

[8] A.D. Anbar, O. Rouxel, Metal stable isotopes in paleoceanography, Annual Review of Earth and Planetary Sciences, 35 (2007) 717-746.

[9] T.D. Bullen, T. Walczyk, Environmental and Biomedical Applications of Natural Metal Stable Isotope Variations, Elements, 5 (2009) 381-385.

[10] F. von Blanckenburg, N. von Wiren, M. Guelke, D.J. Weiss, T.D. Bullen, Fractionation of Metal Stable Isotopes by Higher Plants, Elements, 5 (2009) 375-380.

[11] C.K.I. Sio, N. Dauphas, F.Z. Teng, M. Chaussidon, R.T. Helz, M. Roskosz, Discerning crystal growth from diffusion profiles in zoned olivine by in situ Mg-Fe isotopic analyses, Geochimica Et Cosmochimica Acta, 123 (2013) $^{30}$2-321.

[12] K. Ziegler, E.D. Young, E.A. Schauble, J.T. Wasson, Metal-silicate silicon isotope fractionation in enstatite meteorites and constraints on Earth's core formation, Earth and Planetary Science Letters, $^{29}$5 (2010) 487-496.

[13] T. Hirata, Advances in Laser Ablation–Multi-Collector Inductively Coupled Plasma Mass Spectrometry, in: F. Vanhaecke, P. Degryse (Eds.) Isotopic Analysis: Fundamentals and Applications Using ICP-MS, Wiley-VCH, 2012, pp. 93-112.

[14] F. Albarède, B.L. Beard, Analytical methods for non-traditional isotopes, in: C.M. Johnson, B.L. Beard, F. Albarède (Eds.) Geochemistry of Non-Traditional Stable Isotopes, Mineralogical Society of America, Blacksburg, 2004, pp. 113-152.

[15] I. Horn, F. von Blanckenburg, Investigation on elemental and isotopic fractionation during 196 nm femtosecond laser ablation multiple collector inductively coupled plasma mass spectrometry, Spectrochimica Acta Part B-Atomic Spectroscopy, 62 (2007) 410-422.

[16] J. Marin-Carbonne, M. Chaussidon, M.C. Boiron, F. Robert, A combined in situ oxygen, silicon isotopic and fluid inclusion study of a chert sample from Onverwacht Group (3.35 Ga, South Africa): New constraints on fluid circulation, Chemical Geology, $^{28}$6 (2011) 59-71.

[17] K.B. Knight, N.T. Kita, R.A. Mendybaev, F.M. Richter, A.M. Davis, J.W. Valley, Silicon isotopic fractionation of CAI-like vacuum evaporation residues, Geochimica Et Cosmochimica Acta, 73 (2009) 6390-6401.

[18] J.I. Kimura, Q. Chang, K. Tani, Optimization of ablation protocol for 200 nm UV femtosecond laser in precise U-Pb age dating coupled to multi-collector ICP mass spectrometry, Geochemical Journal, 45 (2011) $^{28}$3-$^{29}$6.

[19] C.C. Garcia, M. Walle, H. Lindner, J. Koch, K. Niemax, D. Gunther, Femtosecond laser ablation inductively coupled plasma mass spectrometry: Transport efficiencies of aerosols released under argon atmosphere and the importance of the focus position, Spectrochimica Acta Part B-Atomic Spectroscopy, 63 (2008) 271-276.

[20] J. Koch, M. Walle, J. Pisonero, D. Gunther, Performance characteristics of ultra-violet femtosecond laser ablation inductively coupled plasma mass spectrometry at similar to 265 and similar to 200 nm, Journal of Analytical Atomic Spectrometry, 21 (2006) 932-940.

[21] M.E. Shaheen, J.E. Gagnon, B.J. Fryer, Femtosecond (fs) lasers coupled with modern ICP-MS instruments provide new and improved potential for in situ elemental and isotopic analyses in the geosciences, Chemical Geology, 3$^{30}$ (2012) 260-273.

[22] J.I. Kimura, Q. Chang, Origin of the suppressed matrix effect for improved analytical performance in determination of major and trace elements in anhydrous silicate samples using 200 nm femtosecond laser ablation sector-field inductively coupled plasma mass spectrometry, Journal of Analytical Atomic Spectrometry, 27 (2012) 1549-1559.

[23] T. Hirata, Advances in Laser Ablation–Multi-Collector Inductively Coupled Plasma Mass Spectrometry, in: Isotopic Analysis, Wiley-VCH, 2012, pp. 93-112.

[24] K.P. Jochum, S.A. Wilson, W. Abouchami, M. Amini, J. Chmeleff, A. Eisenhauer, E. Hegner, L.M. Iaccheri, B. Kieffer, J. Krause, W.F. McDonough, R. Mertz-Kraus, I. Raczek, R.L. Rudnick, D. Scholz, G. Steinhoefel, B. Stoll, A. Stracke, S. Tonarini, D. Weis, U. Weis, J.D. Woodhead, GSD-1G and MPI-DING Reference Glasses for In Situ and Bulk Isotopic Determination, Geostandards and Geoanalytical Research, 35 (2011) 193-226.

[25] J. Chmeleff, I. Horn, G. Steinhoefel, F. von Blanckenburg, In situ determination of precise stable Si isotope ratios by UV-femtosecond laser ablation high-resolution multi-collector ICP-MS, Chemical Geology, 249 (2008) 155-166.

[26] T. Ding, D. Wan, C. Wang, F. Zhang, Silicon isotope compositions of dissolved silicon and suspended matter in the Yangtze River, China, Geochimica Et Cosmochimica Acta, 68 (2004) 205-216.

[27] T.B. Coplen, J.K. Bohlke, P. De Bievre, T. Ding, N.E. Holden, J.A. Hopple, H.R. Krouse, A. Lamberty, H.S. Peiser, K. Revesz, S.E. Rieder, K.J.R. Rosman, E. Roth, P.D.P. Taylor, R.D. Vocke, Y.K. Xiao, Isotope-abundance variations of selected elements - (IUPAC Technical Report), Pure and Applied Chemistry, 74 (2002) 1987-2017.

[28] C. Fitoussi, B. Bourdon, T. Kleine, F. Oberli, B.C. Reynolds, Si isotope systematics of meteorites and terrestrial peridotites: implications for Mg/Si fractionation in the solar nebula and for Si in the Earth's core, Earth and Planetary Science Letters, $^{28}$7 (2009) 77-85.

[29] S. Opfergelt, R.B. Georg, B. Delvaux, Y.M. Cabidoche, K.W. Burton, A.N. Halliday, Silicon isotopes and the tracing of desilication in volcanic soil weathering sequences, Guadeloupe, Chemical Geology, 326 (2012) 113-122.

[30] D.C. Hezel, A.W. Needham, R. Armytage, B. Georg, R.L. Abel, E. Kurahashi, B.J. Coles, M. Rehkamper, S.S. Russell, A nebula setting as the origin for bulk chondrule Fe isotope variations in CV chondrites, Earth and Planetary Science Letters, $^{29}$6 (2010) 423-433.

[31] H.J. Hughes, C. Delvigne, M. Korntheuer, J. de Jong, L. Andre, D. Cardinal, Controlling the mass bias introduced by anionic and organic matrices in silicon isotopic measurements by MC-ICP-MS, Journal of Analytical Atomic Spectrometry, 26 (2011) 1892-1896.

[32] P.S. Savage, R.B. Georg, H.M. Williams, A.N. Halliday, The silicon isotope composition of the upper continental crust, Geochimica Et Cosmochimica Acta, 109 (2013) 384-399.

[33] G. Steinhoefel, J. Breuer, F. von Blanckenburg, I. Horn, D. Kaczorek, M. Sommer, Micrometer silicon isotope diagnostics of soils by UV femtosecond laser ablation, Chemical Geology, $^{28}$6 (2011) $^{28}$0-$^{28}$9.

[34] S. van den Boorn, P.Z. Vroon, M.J. van Bergen, Sulfur-induced offsets in MC-ICP-MS silicon-isotope measurements, Journal of Analytical Atomic Spectrometry, 24 (2009) 1111-1114.

[35] S. van den Boorn, P.Z. Vroon, C.C. van Belle, B. van der Wagt, J. Schwieters, M.J. van Bergen, Determination of silicon isotope ratios in silicate materials by high-resolution MC-ICP-MS using a sodium hydroxide sample digestion method, Journal of Analytical Atomic Spectrometry, 21 (2006) 734-742.
[36] T. Zambardi, F. Poitrasson, Precise Determination of Silicon Isotopes in Silicate Rock Reference Materials by MC-ICP-MS, Geostandards and Geoanalytical Research, 35 (2011) 89-99.
[37] K. Abraham, S. Opfergelt, F. Fripiat, A.J. Cavagna, J.T.M. de Jong, S.F. Foley, L. Andre, D. Cardinal, delta($^{30}$)Si and delta($^{29}$)Si determinations on USGS BHVO-1 and BHVO-2 reference materials with a new configuration on a nu plasma multi-collector ICP-MS, Geostandards and Geoanalytical Research, 32 (2008) 193-202.
[38] R.M.G. Armytage, R.B. Georg, P.S. Savage, H.M. Williams, A.N. Halliday, Silicon isotopes in meteorites and planetary core formation, Geochimica Et Cosmochimica Acta, 75 (2011) 3662-3676.
[39] R. Chakrabarti, S.B. Jacobsen, Silicon isotopes in the inner Solar System: Implications for core formation, solar nebular processes and partial melting, Geochimica Et Cosmochimica Acta, 74 (2010) 6921-6933.
[40] K.P. Jochum, U. Weis, B. Stoll, D. Kuzmin, Q.C. Yang, I. Raczek, D.E. Jacob, A. Stracke, K. Birbaum, D.A. Frick, D. Gunther, J. Enzweiler, Determination of Reference Values for NIST SRM 610-617 Glasses Following ISO Guidelines, Geostandards and Geoanalytical Research, 35 (2011) 397-4$^{29}$.
[41] J.E. Reid, B.T. Poe, D.C. Rubie, N. Zotov, M. Wiedenbeck, The self-diffusion of silicon and oxygen in diopside (CaMgSi2O6) liquid up to 15 GPa, Chemical Geology, 174 (2001) 77-86.
[42] B. Stoll, K.P. Jochum, K. Herwig, M. Amini, M. Flanz, B. Kreuzburg, D. Kuzmin, M. Willbold, J. Enzweiler, An automated iridium-strip heater for LA-ICP-MS bulk analysis of geological samples, Geostandards and Geoanalytical Research, 32 (2008) 5-26.
[43] A.B. Jeffcoate, T. Elliott, S.A. Kasemann, D. Ionov, K. Cooper, R. Brooker, Li isotope fractionation in peridotites and mafic melts, Geochimica Et Cosmochimica Acta, 71 (2007) 202-218.
[44] T. Hewawasam, F. von Blanckenburg, J. Bouchez, J.L. Dixon, J.A. Schuessler, R. Maekeler, Slow advance of the weathering front during deep, supply-limited saprolite formation in the tropical Highlands of Sri Lanka, Geochimica Et Cosmochimica Acta, 118 (2013) 202-2$^{30}$.
[45] F. Poitrasson, X.L. Mao, S.S. Mao, R. Freydier, R.E. Russo, Comparison of ultraviolet femtosecond and nanosecond laser ablation inductively coupled plasma mass spectrometry analysis in glass, monazite, and zircon, Analytical Chemistry, 75 (2003) 6184-6190.
[46] J. Gonzalez, C.Y. Liu, X.L. Mao, R.E. Russo, UV-femtosecond laser ablation-ICP-MS for analysis of alloy samples, Journal of Analytical Atomic Spectrometry, 19 (2004) 1165-1168.
[47] R. Freydier, F. Candaudap, F. Poitrasson, A. Arbouet, B. Chatel, B. Dupre, Evaluation of infrared femtosecond laser ablation for the analysis of geomaterials by ICP-MS, Journal of Analytical Atomic Spectrometry, 23 (2008) 702-710.
[48] R.B. Georg, B.C. Reynolds, M. Frank, A.N. Halliday, New sample preparation techniques for the determination of Si isotopic compositions using MC-ICPMS, Chemical Geology, 235 (2006) 95-104.
[49] C.O. O'Connor, B.L. Sharp, P. Evans, On-line additions of aqueous standards for calibration of laser ablation inductively coupled plasma mass spectrometry: theory and comparison of wet and dry plasma conditions, Journal of Analytical Atomic Spectrometry, 21 (2006) 556-565.
[50] F. Claverie, B. Fernandez, C. Pecheyran, J. Alexis, O.F.X. Donard, Elemental fractionation effects in high repetition rate IR femtosecond laser ablation ICP-MS analysis of glasses, Journal of Analytical Atomic Spectrometry, 24 (2009) 891-902.
[51] J. Fietzke, V. Liebetrau, D. Guenther, K. Gurs, K. Hametner, K. Zumholz, T.H. Hansteen, A. Eisenhauer, An alternative data acquisition and evaluation strategy for improved isotope ratio precision using LA-MC-ICP-MS applied to stable and radiogenic strontium isotopes in carbonates, Journal of Analytical Atomic Spectrometry, 23 (2008) 955-961.
[52] T.H. Her, R.J. Finlay, C. Wu, E. Mazur, Femtosecond laser-induced formation of spikes on silicon, Applied Physics A -Materials Science & Processing, 70 (2000) 383-385.
[53] V. Hommes, M. Miclea, R. Hergenroder, Silicon surface morphology study after exposure to tailored femtosecond pulses, Applied Surface Science, 252 (2006) 7449-7460.
[54] J. Bonse, J.M. Wrobel, J. Kruger, W. Kautek, Ultrashort-pulse laser ablation of indium phosphide in air, Applied Physics A - Materials Science & Processing, 72 (2001) 89-94.
[55] F.X. d'Abzac, F. Poitrasson, R. Freydier, A.M. Seydoux-Guillaume, Near Infra Red femtosecond Laser Ablation: the influence of energy and pulse width on the LA-ICP-MS analysis of monazite, Journal of Analytical Atomic Spectrometry, 25 (2010) 681-689.
[56] S.E. Jackson, D. Gunther, The nature and sources of laser induced isotopic fractionation in laser ablation-multicollector-inductively coupled plasma-mass spectrometry, Journal of Analytical Atomic Spectrometry, 18 (2003) 205-212.
[57] S.J.G. Galer, R.K. O'Nions, Chemical and Isotopic Studies of Ultramafic Inclusions from the San Carlos Volcanic Field, Arizona: A Bearing on their Petrogenesis, Journal of Petrology, $^{30}$ (1989) 1033-1064.
[58] F.A. Frey, M. Prinz, Ultramafic inclusions from San Carlos, Arizona: Petrologic and geochemical data bearing on their petrogenesis, Earth and Planetary Science Letters, 38 (1978) 1$^{29}$-176.
[59] T. Hirata, Y. Hayano, T. Ohno, Improvements in precision of isotopic ratio measurements using laser ablation-multiple collector-ICP-mass spectrometry: reduction of changes in measured isotopic ratios, Journal of Analytical Atomic Spectrometry, 18 (2003) 1$^{28}$3-1$^{28}$8.
[60] I. Kroslakova, D. Gunther, Elemental fractionation in laser ablation-inductively coupled plasma-mass spectrometry: evidence for mass load induced matrix effects in the ICP during ablation of a silicate glass, Journal of Analytical Atomic Spectrometry, 22 (2007) 51-62.
[61] G. Steinhoefel, I. Horn, F. von Blanckenburg, Matrix-independent Fe isotope ratio determination in silicates using UV femtosecond laser ablation, Chemical Geology, 268 (2009) 67-73.
[62] R. Schoenberg, F. von Blanckenburg, An assessment of the accuracy of stable Fe isotope ratio measurements on samples with organic and inorganic matrices by high-resolution multicollector ICP-MS, International Journal of Mass Spectrometry, 242 (2005) 257-272.
[63] N. Dauphas, A. Pourmand, F.Z. Teng, Routine isotopic analysis of iron by HR-MC-ICPMS: How precise and how accurate?, Chemical Geology, 267 (2009) 175-184.
[64] H. Longerich, D. Guenther, S. Jackson, Elemental fractionation in laser ablation inductively coupled plasma mass spectrometry, Fresenius' J. Anal. Chem. 355 (1996) 538–542.
[65] P.S. Savage, R.M.G. Armytage, R.B. Georg, A.N. Halliday, High temperature silicon isotope geochemistry, Lithos, 190–191 (2014) 500-519.
[66] I. Gunther-Leopold, B. Wernli, Z. Kopajtic, D. Gunther, Measurement of isotope ratios on transient signals by MC-ICP-MS, Analytical and Bioanalytical Chemistry, 378 (2004) 241-249.
[67] T. Pettke, F. Oberli, A. Audetat, U. Wiechert, C.R. Harris, C.A. Heinrich, Quantification of transient signals in multiple collector inductively coupled plasma mass spectrometry: accurate lead isotope ratio determination by laser ablation of individual fluid inclusions, Journal of Analytical Atomic Spectrometry, 26 (2011) 475-492.
[68] A. Shahar, E.D. Young, Astrophysics of CAI formation as revealed by silicon isotope LA-MC-ICPMS of an igneous CAI, Earth and Planetary Science Letters, 257 (2007) 497-510.
[69] P.J. Potts, Glossary of Analytical and Metrological Terms from the International Vocabulary of Metrology (2008), Geostandards and Geoanalytical Research, 36 (2012) 231-246.
[70] VIM, International vocabulary of metrology – Basic and general concepts and associated terms (VIM), 2008, 90 pp. and Corrigendum (May 2010).
[71] I. Horn, F. von Blanckenburg, R. Schoenberg, G. Steinhoefel, G. Markl, In situ iron isotope ratio determination using UV-femtosecond laser ablation with application to hydrothermal ore formation processes, Geochimica Et Cosmochimica Acta, 70 (2006) 3677-3688.
[72] G. Steinhoefel, F. von Blanckenburg, I. Horn, K.O. Konhauser, N.J. Beukes, J. Gutzmer, Deciphering formation processes of banded iron formations from the Transvaal and the Hamersley successions by combined Si and Fe isotope analysis using UV femtosecond laser ablation, Geochimica Et Cosmochimica Acta, 74 (2010) 2677-2696.
[73] K. Ikehata, K. Notsu, T. Hirata, In situ determination of Cu isotope ratios in copper-rich materials by NIR femtosecond LA-MC-ICP-MS, Journal of Analytical Atomic Spectrometry, 23 (2008) 1003-1008.

[74] P.J. le Roux, S.B. Shirey, L. Benton, E.H. Hauri, T.D. Mock, In situ, multiple-multiplier, laser ablation ICP-MS measurement of boron isotopic composition (delta B-11) at the nanogram level, Chemical Geology, 203 (2004) 123-138.
[75] M. Tiepolo, C. Bouman, R. Vannucci, J. Schwieters, Laser ablation multicollector ICPMS determination of delta B-11 in geological samples, Applied Geochemistry, 21 (2006) 788-801.
[76] J. Fietzke, A. Heinemann, I. Taubner, F. Bohm, J. Erez, A. Eisenhauer, Boron isotope ratio determination in carbonates via LA-MC-ICP-MS using soda-lime glass standards as reference material, Journal of Analytical Atomic Spectrometry, 25 (2010) 1953-1957.
[77] K.J. Hou, Y.H. Li, Y.K. Xiao, F. Liu, Y.R. Tian, In situ boron isotope measurements of natural geological materials by LA-MC-ICP-MS, Chinese Science Bulletin, 55 (2010) 3$^{30}$5-3311.
[78] P.J. le Roux, Lithium isotope analysis of natural and synthetic glass by laser ablation MC-ICP-MS, Journal of Analytical Atomic Spectrometry, 25 (2010) 1033-1038.
[79] E.D. Young, J.I. Simon, A. Galy, S.S. Russell, E. Tonui, O. Lovera, Supra-canonical Al-26/Al-27 and the residence time of CAIs in the solar protoplanetary disk, Science, $^{30}$8 (2005) 223-227.
[80] E.D. Young, E. Tonui, C.E. Manning, E. Schauble, C.A. Macris, Spinel-olivine magnesium isotope thermometry in the mantle and implications for the Mg isotopic composition of Earth, Earth and Planetary Science Letters, $^{28}$8 (2009) 524-533.
[81] J. Kosler, R.B. Pedersen, C. Kruber, P.J. Sylvester, Analysis of Fe isotopes in sulfides and iron meteorites by laser ablation high-mass resolution multi-collector ICP mass spectrometry, Journal of Analytical Atomic Spectrometry, 20 (2005) 192-199.
[82] S. Graham, N. Pearson, S. Jackson, W. Griffin, S.Y. O'Reilly, Tracing Cu and Fe from source to porphyry: in situ determination of Cu and Fe isotope ratios in sulfides from the Grasberg Cu-Au deposit, Chemical Geology, 207 (2004) 147-169.
[83] R. Hergenroder, O. Samek, V. Hommes, Femtosecond laser ablation elemental mass spectrometry, Mass Spectrometry Reviews, 25 (2006) 551-572.
[84] D.R. Lide, CRC Handbook of Chemistry and Physics, 90th Edition, CRC Press, 2010.
[85] R. Glaus, R. Kaegi, F. Krumeich, D. Gunther, Phenomenological studies on structure and elemental composition of nanosecond and femtosecond laser-generated aerosols with implications on laser ablation inductively coupled plasma mass spectrometry, Spectrochimica Acta Part B-Atomic Spectroscopy, 65 (2010) 812-822.
[86] F.X. D'Abzac, A.M. Seydoux-Guillaume, J. Chmeleff, L. Datas, F. Poitrasson, In situ characterization of infra red femtosecond laser ablation in geological samples. Part B: the laser induced particles, Journal of Analytical Atomic Spectrometry, 27 (2012) 108-119.
[87] F.X. d'Abzac, B.L. Beard, A.D. Czaja, H. Konishi, J.J. Schauer, C.M. Johnson, Iron Isotope Composition of Particles Produced by UV-Femtosecond Laser Ablation of Natural Oxides, Sulfides, and Carbonates, Analytical Chemistry, 85 (2013) 11885-11892.
[88] S. Opfergelt, P. Delmelle, Silicon isotopes and continental weathering processes: Assessing controls on Si transfer to the ocean, Comptes Rendus Geoscience, 344 (2012) 723-738.